Study on refractory high-entropy alloys for nuclear fusion application

北海道大学
HOKKAIDO UNIVERSITY

A thesis submitted in partial fulfillment for the degree of doctor of philosophy

Yun ZONG

Graduate School of Engineering

Hokkaido University

Acknowledgements

At the end of my studies at Hokkaido University, I want to express my heartfelt gratitude to everyone who supported me with invaluable support during my Ph.D. studies here over three years. I know very well that I cannot get a Ph.D. without their help.

Firstly, I would like to express my great thanks to my supervisor, Professor Naoyuki Hashimoto, for giving me the chance to study for a doctorate. Even I am not a student who can meet the expectations, I want to thank him for providing me kind guidance and good suggestions with my research work. I'm also very grateful for his kind consideration during the COVID period.

Secondly, I would like to give my hearty thanks to Professor Shigehito Isobe, Professor Seiji Miura, and Professor Munekazu Ohno. Professor Isobe, thank him for helping me during my Ph.D. research. Not only did he provide research assistance, but he also always gave me confidence. Professor Seiji Miura is an erudite professor of more knowledge. I am grateful to him for sharing knowledge in the HEAs field, spending his time on discussion. Professor Ohno, I wish to express my appreciation to him for help with my graduation. He is mighty and modest in my mind.

Thirdly, I would like to thank secretary Kaori Kobayashi for providing my study and life with all kinds of assistance over the three years. I am indebted to assistant professor Hiroshi Oka for his helpful discussion and constructive suggestions. I also would like to express my appreciation to the members of the laboratory of Nano-Mirco Materials Analysis (NMA) for their support on the use of instruments. Special thanks to Specially Appointed Assistant Professor Yongming Wang for giving me TEM training and helping me whenever I encounter problems.

I also owe my sincere gratitude to all the former and present students in LOAM. It is very grateful that everyone communicated with me enthusiastically, helped me solve problems in experiments and life. Much gratitude for the warmth you gave to me in a foreign land.

Lastly, my thanks would go to my beloved father and mother for their loving considerations of me all through three years, even I can not come back to China for quite a long time, they always give me support mentally and financially. Without them, I could not go through the tough homesick period. Also, I want to express my great thanks to my beautiful, lovely, and gorgeous friends: Xinxin Liu, Qi Kan, Mengke Niu, and Shiyao Wang. Thank you for giving me kind help during the daily life and support me when I feel upset. It is a happy time to spend with you during the doctor's study.

Abstract

Nowadays, more and more researchers have paid attention to nuclear power because of its high production efficiency. With a performance target for the next 20 years, scientists start to work on controlling nuclear fusion to make a fusion reactor since the releasing energy of fusion is several times the amount produced from fission. As the important part of fusion reactor ITER, diverter, the materials designed for it require special properties that could survive at high temperatures, high corrosion, and high irradiation environment. After a few years of development, Carbon-fiber composite (CFC) and tungsten have become the candidate materials for the ITER divertor, but both kinds of materials have disadvantages. Considering this, high-entropy alloys with Ti, Zr, Hf, Ta, V, Nb, W, and Cr may be a good candidate which can replace pure tungsten in the future. In this research, MoNbTaTi, MoNbTaW, MoNbTaTiW, HfNbTaTiZr and HfNbTaTiV high-entropy alloy was investigated with a special focus on the irradiation hardening and microstructure.

First of all, we developed body-centered cubic refractory high-entropy alloys, MoNbTaTi, MoNbTaW, and MoNbTaTiW, and explored their microstructure, and mechanical properties in order to develop a new high-irradiation resistance material suitable for fusion reactor components. Three HEAs were annealed at 1200°C for 48 hours to form single face BCC alloys, while MoNbTaW was also annealed at 1500°C. SEM inspection and EDS mapping have both validated this result. The Vickers hardness of three HEAs was investigated, and the stable results indicate that they are all stable at elevated temperatures. Three HEAs are ion irradiated with 6.4 MeV Fe^{3+} at a temperature of 500°C, and the irradiation hardening is examined using nanoindentation. In comparison to pure tungsten, the three HEAs exhibit increased resistance to irradiation.

Secondly, based on Senkov alloy, which has been identified as BCC alloys with good ductility, this work developed the HfNbTaTiV, and explored its microstructure, and mechanical properties to make a comparison between F82H and Senkov alloy (HfNbTaTiZr). The phase diagram of HfNbTaTiV indicates that this alloy is stable with a single BCC matrix the temperature above 800°C. The mechanicapropertiesed including Vickers hardness and the tensile property has been conducted to HfNbTaTiV, Senkov alloy, and F82H. The results indicate that HfNbTaTiV has higher Vickers hardness than Senkov alloy, and the yield stress and tensile strength of HfNbTaTiV are larger than that of Senkov alloy and F82H, while elongation was found to be larger in the order of HfNbTaTiV, Senkov alloy, and F82H. Three HEAs are ion irradiated with 6.4 MeV Fe^{3+} at a temperature of 300°C, the irradiation hardening of Senkov alloy is larger than that of HfNbTaTiV and F82H. However, the TEM observation represents different results and the possibilities of this phenomenon will be discussed in this work.

Table of contents

List of Figures

List of Tables

Chapter 1

Introduction

1.1 Energy in the world

Energy is the primary ‘fuel’ for social and economic development; people have been using energy from nature like wind power, solar power, and hydropower for thousands of years. With technology developing, the efficiency of energy utilization has made great progress. The energy resources can be divided into two categories: nonrenewable energy resources and renewable energy resources. Non-renewable energy comes from sources that will run out or will not be replenished in our lifetimes. Nonrenewable energy resources like coal, soil, and natural gas, are with limited supplies.[1] Renewable resources can be replenished naturally with a short period. The five major renewable energy resources are solar, wind (hydro), biomass, and geothermal. It is still under debating whether nuclear energy should be renewable energy since uranium and plutonium could not be replenished within a natural process.

As we can see in figure 1.1, fossil fuels like petroleum, coal, and natural gas make up a large portion of today’s energy market; more and more fossil fuels are utilized into electricity and car industry. It is believed that fossil fuel could lead to global warming because of the releasing of carbon dioxide and the greenhouse effect. Global warming is regarded to cause extreme weather which leads to severe climate disasters like heat waves, droughts, and floods.[2] In order to protect the environment, renewable energy was developed to release the pressure of fossil energy supply and environment pollution. According to the survey results, there are 34% of the world’s electricity production from fission and renewable energy by 2012 [3].

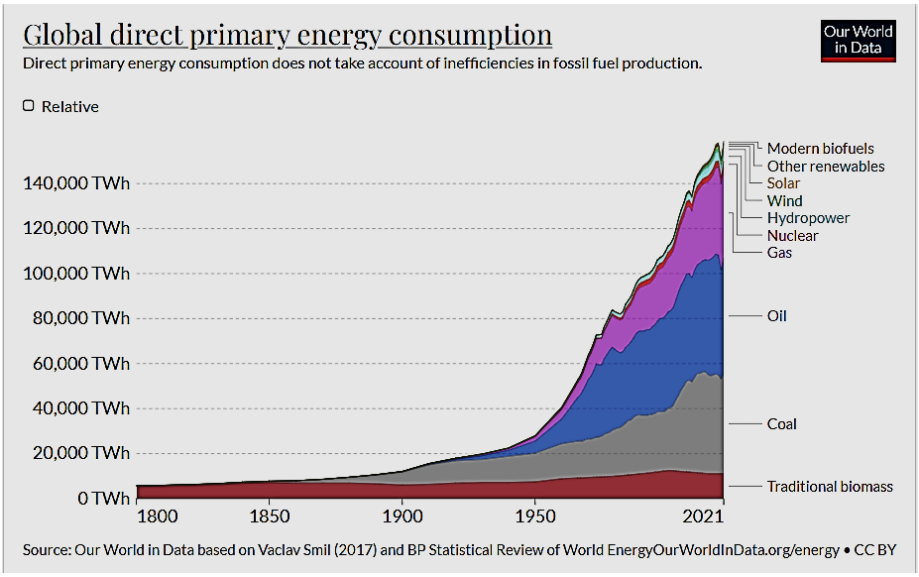

Fig. 1.1 Primary energy consumption by the source of the world

1.2 Nuclear energy and reactor

Nowadays, more and more researchers have paid attention to nuclear power because of its high production efficiency. Nuclear power can be obtained from nuclear fission, nuclear decay and nuclear fusion reactions. [4] At present, nuclear energy systems have required a great deal of expertise through the operation of reactors from generation I to generation III. All commercial power reactors are based on nuclear fission reaction. As of 2014, 93% of the world's nuclear reactors are water cooled, providing about 95% of the world's total nuclear generation capacity, which includes Pressurized water reactor (PWR), Boiling water reactor (BWR), pressurized heavy-water reactor (PHWR), and some other reactors. [5]

With a performance target for the next 20 years, scientists start to work on controlling nuclear fusion to make a fusion reactor since the releasing energy of fusion is several times the amount produced from fission. Fusion energy is a kind of energy that could generate electricity by using heat from nuclear fusion reactions. During the fusion process, two lighter atomic nuclei (such as deuterium or tritium) combine to form a heavier nucleus and then release energy. Scientists start to work on controlling nuclear fusion reactor since the releasing energy is several times the amount produced from fission. Fusion energy is an ideal candidate for future energy supply with less pollution. The sufficient energy sources like deuterium comes from the nature while tritium is breading from lithium, and neutron reaction. [6,7]

The reactions could be described as:

$$D + T \rightarrow {}^{4}He + n + 14.1MeV \quad \text{(eq. 1-1)}$$

$${}^{6}Li + n \rightarrow T + 4.8MeV \quad \text{(eq. 1-2)}$$

$${}^{7}Li + n \rightarrow T + n - 2.5MeV \quad \text{(eq. 1-3)}$$

In order to put fusion energy into commercial application, devices designed to harness this energy are known as fusion reactors. Various countries in the world like US, EU,

Japan, China, Russia, Korea, and India started to build the largest experimental nuclear fusion reactor named the International Thermonuclear Experimental Reactor (ITER), as shown in Fig. 1.1. Ignition of plasma requires high temperature. [8,9]

To extract the helium waste, the plasma was designed to hit the bottom of the blanket which is called divertor. The divertor is a region of the plasma where the outer magnetic field lines are opened (join up with the wall or a different part of the vacuum vessel) [10].

The divertor has three functions: (1) helium trashes extraction, (2) fuel recycle, (3) heat exchange.

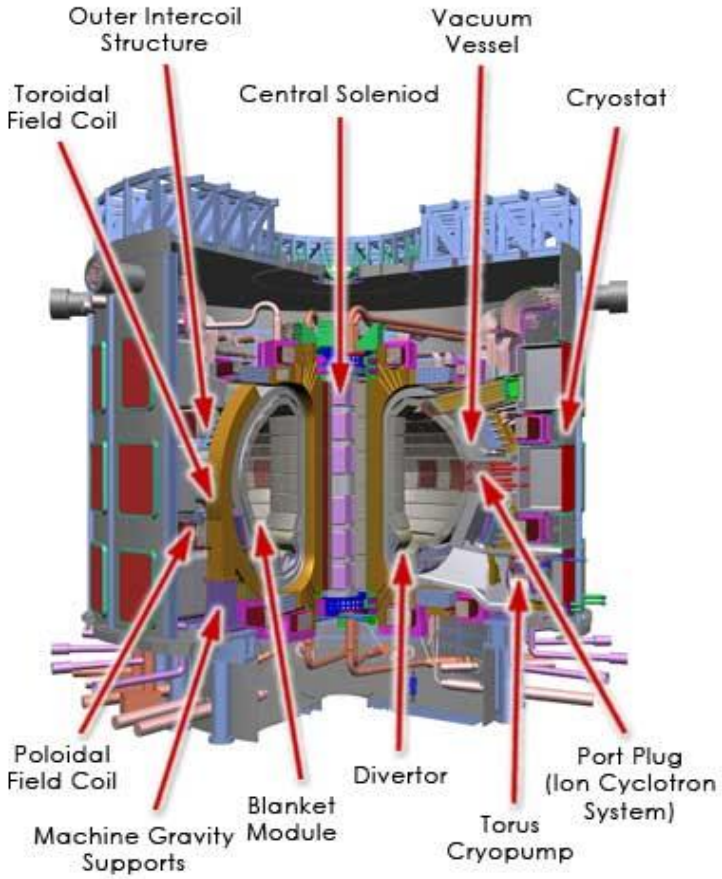

Fig 1.2 The schematic structure of ITER [11].

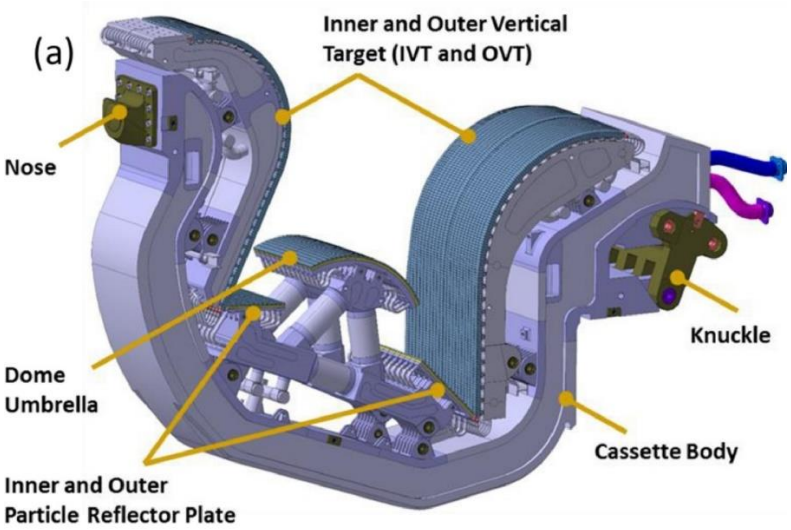

Fig 1.3 The schematic structure of divertor in ITER.

1.3 A short overview of nuclear materials

Over recent decades, many materials utilized in nuclear reactors have been developed by researchers such as Ti, Fe, Zr alloys, ZrO_2 Ni-alloys, low-alloy ferritic-steel, and SiC-based ceramics. [12] As we mentioned above, as the key part in fusion reactor, the divertor has to experience the extreme environment such as high heat and heavy energetic bombard. Therefore, the materials designed for divertor require special properties that could survive at high temperature, high corrosion, and high irradiation environment. At the same time, the materials should also have good conductivity to make sure the efficiency of energy conversion and superior sputtering resistance to prevent the atoms falling into the plasma which will lower the temperature greatly under ignition condition.

Early candidate refractory metals for plasma facing materials include Ta and Mo alloys with good performances in high temperature strength and ductility [13]. After few years development, Carbon-fiber composite (CFC) and tungsten has become the candidate materials for the ITER divertor. Both materials have positive and negative properties in application. Due to its strong conductivity, CFC can withstand high heat loads. If overheated during disruption events, it will dissipate, and the behavior of a melt layer is unimportant. The use of CFC further lessens issues if divertor misalignment occurs and the leading edges of the SOL are intercepted (Flux approximately 100MW/m2). [10]. However, the carbon (carbon fibre composite, CFC) has a problem with heavy fuel retention, and carbon and hydrogen frequently create strong chemical bonds. This could lead to large Tritium accumulation in dust in the divertor region. [14, 15]. W has attracted significant emphasis as an ideal material for in-vessel components such as diverters and blankets in a fusion reactor because of its high-temperature capabilities and low sputtering yield. However, tungsten's inherent brittleness at low temperatures and irradiation embrittlement have precluded its usage in fusion reactor applications. Considering this, high-entropy alloys with Ti, Zr, Hf, Ta, V, Nb, W, and Cr may be a good candidate which can replace the pure tungsten in the future. There are no

literatures related to the research of refractory HEAs for fusion reactor, hope this research will give a good advice for the development of HEAs which can be used in fusion reactors.

1.4 High-entropy alloy

In order to promote living conditions, people have started to develop new materials, especially new alloys. As we all know, alloys have played an important role in people's daily lives for more than thousands of years. These conventional alloys are traditionally developed based on one principal element. To improve their properties, various elements are added to the alloy to form new alloy family. Generally, base element accounts for more than 80% of the total formulation so the base element dominates the chemistry properties of alloys [16]. Researchers developed the single alloys with more than 12 elements recently, which defined as superalloys, still contains more than 50% of the principal element. Only in comparatively rare cases, superalloys are consisted with roughly 20% of each transition metal elements. However, superalloys always also own complex crystal structures which would lead to a reduction in corrosion resistance, microstructure stability, and mechanical properties [17, 18].

Considering this, within the past several years, researchers have focused on a fundamentally new alloying concept. The new alloy is defined as high-entropy alloys (HEAs), which combines n ($n \geqslant 5$) elements of roughly equimolar concentrations [19]. HEAs have attracted great research interest in the field of materials science and engineering recently. As we all know, conventional alloys always contain one and rarely two base elements, while HEAs contains multiple principal elements, which extends the whole research field of alloys.

According to Fig. 1.4, researchers previously only focused on the designing conventional alloys, which occupies a small part of designing space [20]. With the advent of HEAs, researchers' concentration can be changed to the HEAs in the central region. Typically, this is a huge creation from conventional theories, opening up new avenues of alloy design to be explored in depth. In the literature, Yeh gave two definitions for HEAs, one is based on chemical composition, that HEAs are formed by

containing n principle elements of roughly equimolar concentrations (n⩾5). If n is large, the high entropy of mixing elements can stabilize the phases with quite simple crystal structures instead of forming the complex intermetallic phases. Therefore, unlike superalloys, high-entropy alloys may have complex compositions, but they have simple microstructure. The other definition is based on configurational entropy, that HEAs are defined as alloys having configurational entropies at a random state $> 1.36R$ or $> 1.5R$ (R is the ideal gas constant), despite they are single phase or multiphase. [21] In order to increase the number of HEAs during the design process, HEAs can also contain minor elements to change the properties of the HEA base. [22] Clearly, this concept offers many opportunities to discover and develop new families of alloys including high strength alloys, high-temperature alloys, and light metal alloys, for structural and functional applications.

The HEA research field presents new ideas to explore the vast realm of hyper-dimensional complex composition space and to manage configurational entropy by alloy composition in order to favor solid solution alloys. Solid solution hardening is an important reinforcement mechanism, and according to the literature, intermetallic phase alloys are highly brittle and make process difficult. While solid solution alloys are engineered to be strong and maintain damage tolerance and ductility. [22,23] Considering this, the HEA area will attract more and more focus for sing-phase solid solutions' research.

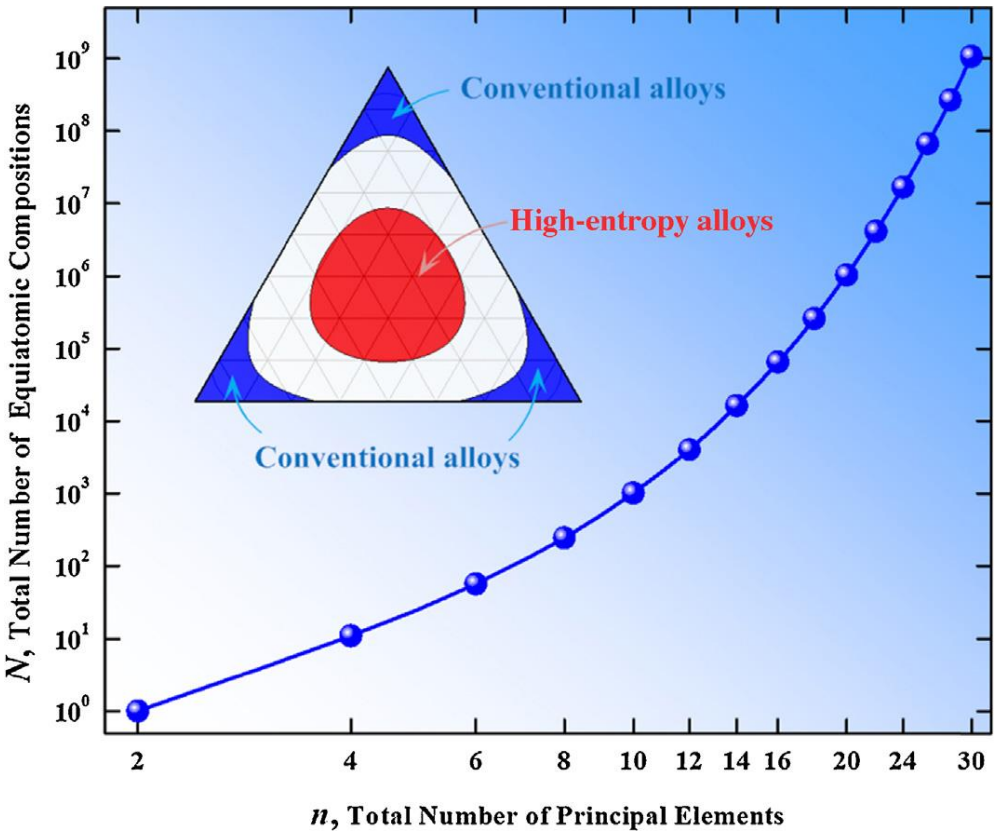

Fig. 1.4 The variation in the total number of equiatomic compositions with the total number of principal elements. The inset illustrates the difference between the design of conventional alloys and high-entropy alloys on a ternary plot [20].

1.5.1 Core effects of HEAs

1.5.1.1 High-Entropy Effect.

The high-entropy effect mainly describes that the higher entropy in HEAs lowers the free energy of solid solution phases and provides the simple structure, especially at higher temperatures. [24, 25] Because of the mutual solubility among constituent elements, the number of phases in HEAs that we can developed can be reduced to some extent.

According to the formula:

$G = H - TS$ (eq.1-4) [26]

G: Gibbs free energy

H: enthalpy

T: temperature

S: entropy

if the temperature is high enough, entropy can stabilize the phases of HEAs. In conventional alloys, solid solution phases (including intermediate and terminal solid solutions) have higher mixing entropy than intermetallic compounds. As for HEAs, the difference in entropy between solid solutions and compounds is larger than conventional alloys because of the complex composition. There is also a possibility that solid solution phases become most stable phase at high temperature. In this situation, it is expected that the degree of ordered phase decrease with temperature increasing. Thus, even those alloys contain ordered phases in cast state can transform to solid solutions at high temperature. However, if the formation of an intermetallic compound is strong enough to overcome the effect of entropy, that intermetallic compound will still be more stable at high temperature [27].

1.5.1.2 Sluggish Diffusion Effect.

Within the past few years' research, it was proposed that the phase transformation and diffusion kinetics in HEAs are slower than conventional alloys. This can be understood from two aspects. Firstly, in HEA the neighboring atoms are different from each other. Therefore, for each site, the bonding and local energies are different owing to the different local atomic configuration. The atom has a lower chance to jump out of a low-energy site, while it has a higher chance to jump out of a high-energy chance. The diffusion process slows down in these situations. For example, as shown in Fig. 1.5, the Ni atoms diffused in CoCrFeMnNi which has FCC structure. The mean potential energy difference between lattice sites is higher than that in FeCrNi alloys. Also, as shown in Table 1.1, the activation energy of diffusion in the CoCrFeMnNi alloys is higher than those in pure elements and other FCC alloys. Secondly, the diffusion rate of each element in a HEA is different. Some elements are less active, especially these with high melting points, than others so these elements. Therefore, these elements have lower success rates for jumping into vacancies than other elements. However, phase transformations typically require the coordinated diffusion of many kinds of elements [28].

The slow kinetics in HEAs allows readily nano-sized precipitates and attainable supersaturated state. It also has a good influence on the excellent performance of HEA coatings as diffusion barriers. Because of the same reason, HEAs are also expected to have superior creep resistance.

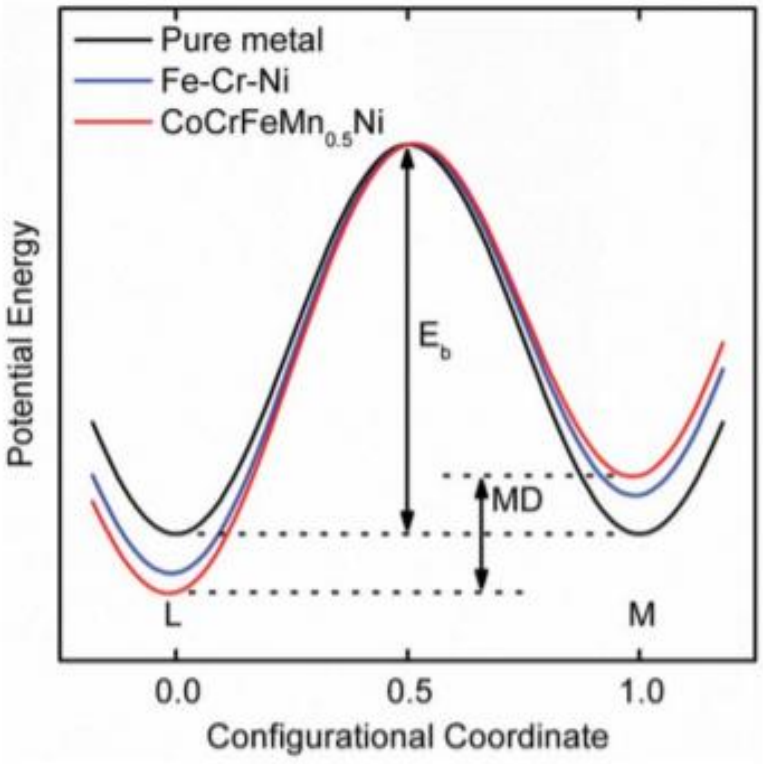

Fig. 1.5 Schematic diagram of the potential energy change during the migration of a Ni atom [28].

Table 1.1

Diffusion parameters for Ni in different FCC matrices. The compositions of Fe-Cr-Ni(-Si) alloys are in wt.% [28].

Solute	System	D_0 (10^{-4} m^2/s)	Q (kJ/mol)	$T_m(T_s)$ (K)	Q/T_m	D_{T_m} (10^{-13} m^2/s)
Ni	CoCrFeMnNi	19.7	317.5	1607	0.1975	0.95
	FCC Fe	3	314	1812	0.1733	2.66
	Co	0.43	282.2	1768	0.1596	1.98
	Ni	1.77	285.3	1728	0.1651	4.21
	Fe-15Cr-20Ni	1.5	300	1731	0.1733	1.33
	Fe-15Cr-45Ni	1.8	293	1697	0.1727	1.73
	Fe-22Cr-45Ni	1.1	291	1688	0.1724	1.09
	Fe-15Cr-20Ni-Si	4.8	310	1705	0.1818	1.53

1.5.1.3 Severe-Lattice-Distortion Effect.

As we mentioned above, high-entropy alloys are composed of various elements, every element has a different size. These size differences lead to lattice distortion. Larger atoms push away other neighboring atoms and small ones have extra space around. The overall free energy of HEA increases because of the strain energy. It also has an influence on the properties of HEAs. For instance, lattice distortion prevents dislocation movement and leads to solid solution strengthening. It also causes an increase in the scattering of propagating phonons and electrons. This would translate to lower thermal and electrical conductivity [25].

1.5.1.4 Cocktail Effect.

The constituent elements have a huge influence on the properties of HEAs. For instance, the addition of elements with high melting points increases the melting points of the alloy. However, besides the properties of the individual composing elements, we should also consider the interaction among the constituent elements. For example, as we all know, Al is a soft element with low-melting-point. However, after the addition of Al, as shown in Fig. 1.6, the harness of high-entropy alloy, $Al_xCoCrCuFeNi$, has increased. It is clear in this figure that the hardness of alloy increases with the addition of Al. There are three reasons to explain this situation including its larger atomic size, the formation of a hard BCC phase, and the stronger cohesive bonding between Al and other elements. Therefore, the mechanical and chemical properties of HEA not only come from the component elements but also include the effects of the interaction among the constituent elements and lattice distortion.

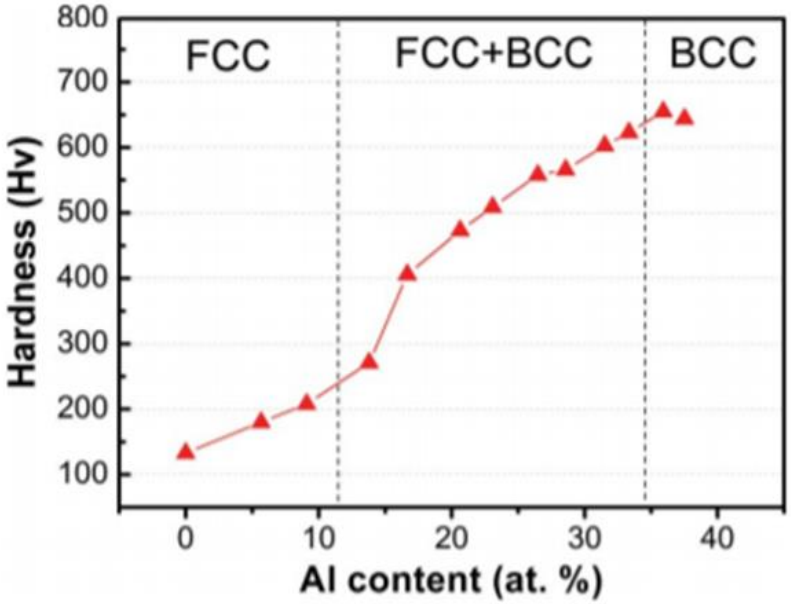

Fig. 1.6 Hardness of the $Al_xCoCrCuFeNi$ alloys as a function of Al content.

1.6 Phase and Crystal Structure of HEAs

The phases of conventional alloys are typically divided into three types: terminal solutions, intermediate solutions, and intermetallic compounds. HEAs can also be classified according to this concept. Terminal phases are based on one principal element. The intermetallic compounds are stoichiometric and have fixed composition ratio. However, because phases in HEAs typically have a composition range instead of fixed composition ratio, there are few intermetallic compounds in HEAs. Solution phases include the solid solutions based on both simple and complex structures [29].

However, according to the literature, phases in HEAs are usually classified a little bit differently. They are often classified as ordered solid solution (e.g. B2 and L12), random solid solution (e.g. FCC, BCC), and intermetallic phases (e.g. Laves phases). Since the intermetallic phases can also be classified as ordered solid solutions—they all have composition ranges and are typically ordered. It is very difficult to distinguish between intermetallic and ordered solid solutions. Therefore, it is easy for us to study on the random solid solution phase of HEA, a phase is simple with FCC, BCC or HCP matrix. Several review papers have been published in aspects of the classifications of HEAs within the past few years. Firstly, Miracle and Senkov reviewed 408 HEA alloys and divide them into three main families, 3d-transition-metal HEAs (constituted by the 3dtransition-metallic elements), refractory metal HEAs (constituted by the refractory-metallic elements), and others [30]. However, after detail research on 3d-transition-metal HEAs, mechanical properties of HEAs are complicated and cannot be classified only as the 3d-trasition-metal HEAs. Therefore, according to the literature, HEA systems are divided into four families for the first time, shown in Fig. 1.7. The first is the soft HEA solid solutions, only including 3d-transition metals. The second is the combination of transition metals with larger-atomic radius elements. The third is based on refractory metals. A few other alloy systems, such as CoCrFeNiPd, MoPdRhRu, and DyGdLuTbY, are also studied [31].

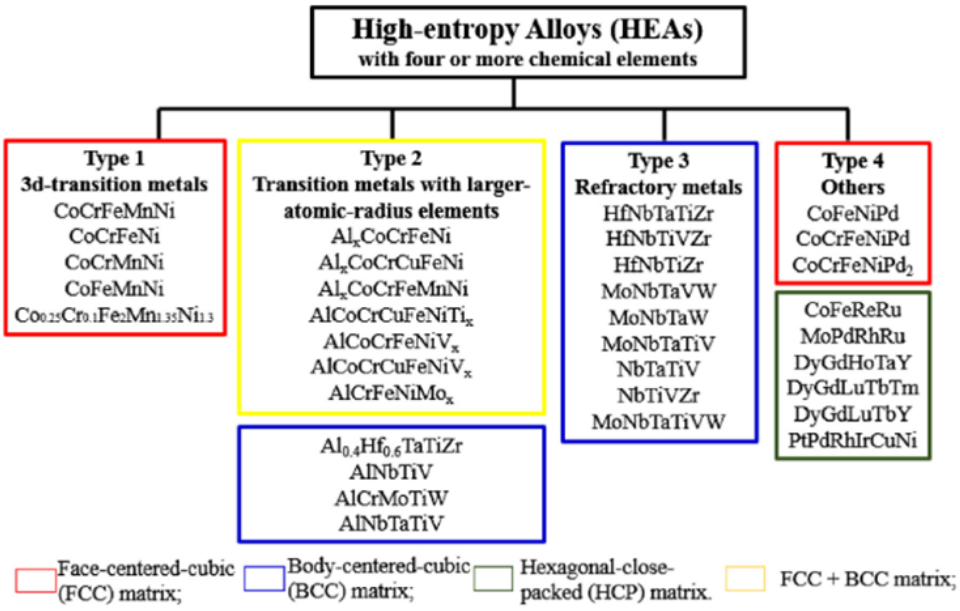

Fig. 1.7 The classifications of high-entropy alloys (HEAs) [31]

1.7 Review of BCC high-entropy alloy

A considerable amount of literature has been published on BCC HEAs which are related with mechanical properties [32,33], corrosion resistance [34,35], oxidation resistance [36,37], compositional gradient films, fibers, and application of high-throughput techniques [38]. Unlike FCC HEAs which have excellent ductility and high plasticity, BCC HEAs can only deal with liquid-solid phase transformation by some processing technology, such as melt purification, homogenization, directional solidification (DS), additive manufacturing (AM) and powder metallurgy (PM). During recent research, it has been proved that simple arc-melting and casting is a highly effective method for fabricating BCC HEAs with more than five metals. When discussing the properties of BCC HEAs, they exhibit relatively high intrinsic yield strengths [39,40]. Besides, RHEA systems have excellent high-temperature mechanical properties but insufficient toughness at room temperature [41,42]. For instance, the AlCrFeCoNi HEA with a single-phase BCC solid solution exhibits excellent compressive properties of yield stress (1250.96 MPa) and plastic strain (32.7%) [43]. Therefore, BCC HEAs show significant potential in future application for nuclear reactors.

1.7.1 Mechanical properties

Mechanical properties are strongly dependent on composition and microstructure. Composition decides elastic properties and atomic interactions which have effect on dislocation behaviors. The composition also determines alloy's phases and their volume fractions which affect their inherent properties.

Figure 1.8 compares the uniaxial deformation behavior of BCC-structured HEAs with typical structural alloys to provide a rather comprehensive overview of their mechanical properties [44]. BCC-structured HEAs are mainly composed of refractory elements, which are commonly used in high-temperature applications. Nb-Ta-Mo-W [45-47], Nb-Ti-Zr [48-50], and Nb-Ti-V [51-53] are examples of successful RHEA systems.

Alloying is also commonly utilized to improve the mechanical properties of HEAs. The most widely utilized alloying elements to improve specific yield strength are refractory elements (Nb, V, and Zr), Ti, and Al with low density. Alloys containing Ti element have good ductility and high-temperature characteristics [54]. At room temperature, for example, the solid-solution hardening effect of Ti addition improves the compressive strength and ductility of MoNbTaW and VMoNbTaW HEAs. TiNbMoTaW and TiVNbMoTaW have yield strengths of 586 and 659 MPa at 1200 °C [54], respectively, and are predicted to be employed as high-temperature materials. In comparison to the addition of V, the addition of Cr causes Laves phase precipitation in the BCC matrix, resulting in strengthening. Furthermore, the structural and mechanical properties of two HEAs remained stable after a short period (10 min) of high-temperature heat treatment, as shown in Figure 1.9. Substituting Hf and Cr in the $CrMo_{0.5}NbTa_{0.5}TiZr$ and HfNbTaTiZr HEAs can reduce density while improving RT strength and ductility [55].

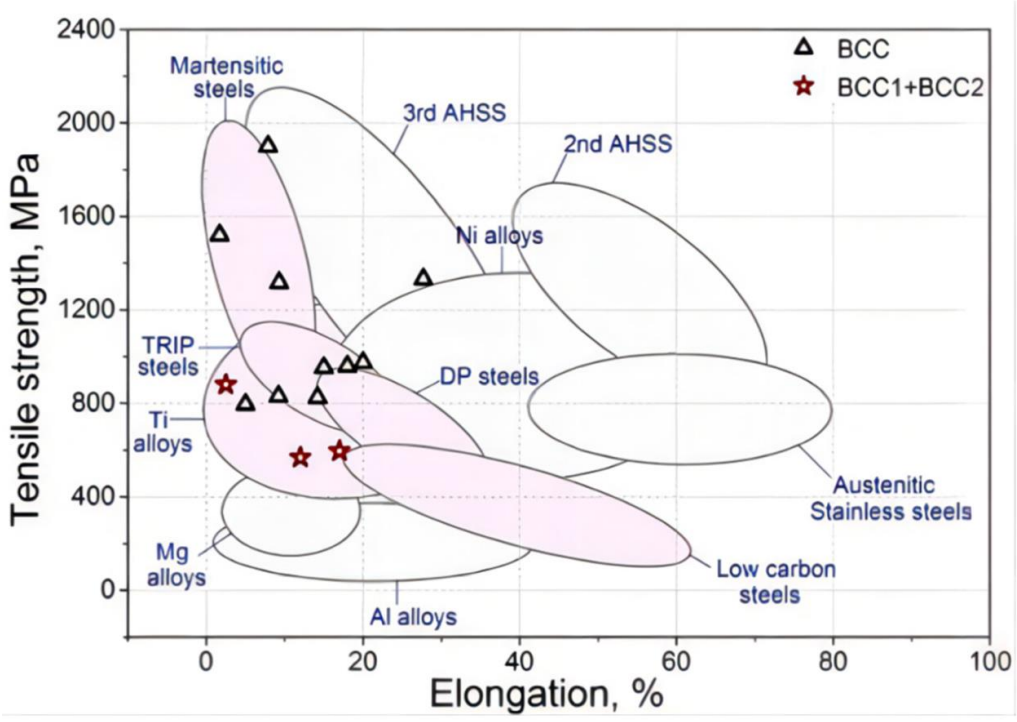

Fig. 1.8 Room-temperature uniaxial tension test data of HEAs and CCAs with BCC, BCC1 + BCC2, 2nd and 3rd AHSS stand for the two generations of advanced high-strength steels

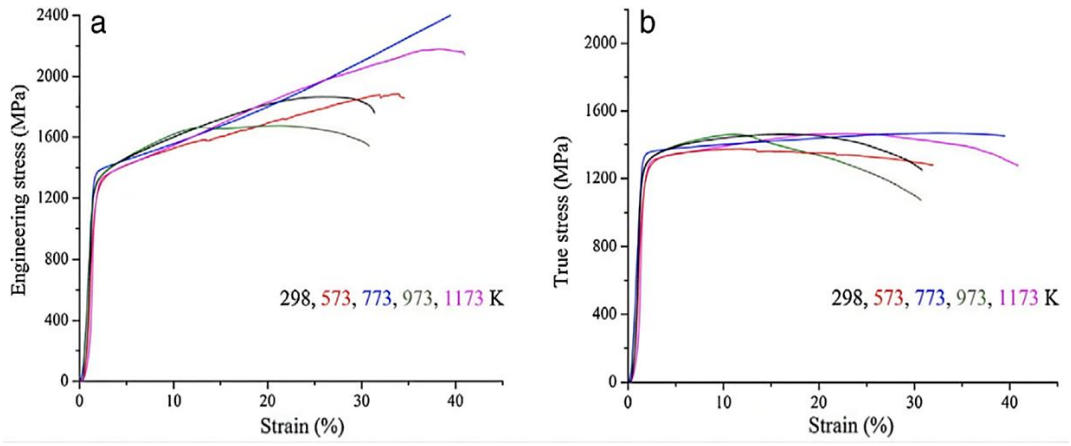

Fig. 1.9 Engineering stress and true stress vs. strain compression curves for the Ti20Zr20Hf20Nb20V20 (a,b) and Ti20Zr20Hf20Nb20Cr20 alloys in the as-cast1.7.2

1.7.2 Thermal conductivity

The body-centered cubic (BCC) HEAs are particularly crucial for high-temperature applications. Therefore, the refractory metals are the primary constituents for the designing process. Also, the refractory MEAs/HEAs are known for their superior thermal stability and low thermal conductivity κ, which could be attributed to the sluggish diffusion that prevents the grain-growth [56,57] and the severe lattice distortion which enhances the phonon/electron scattering. At the same time, there remains the question whether those two effects influence the thermal stability and thermal/electrical transport properties.

Thermal conductivity of any material is dependent on two things: motion of free electrons and molecular vibrations. For metals, the thermal conductivity is mainly a function of the motion of free electrons. As the temperature increases, the molecular vibrations increase (in turn decreasing the mean free path of molecules). So, they obstruct the flow of free electrons, thus reducing the conductivity. Figure 1.10 shows the thermal conductivity of several BCC HEAs, and the results indicate that the thermal conductivity of BCC HEAs increase with the temperature raising. [58] Therefore, BCC HEAs will have significant potential in high-temperature environment.

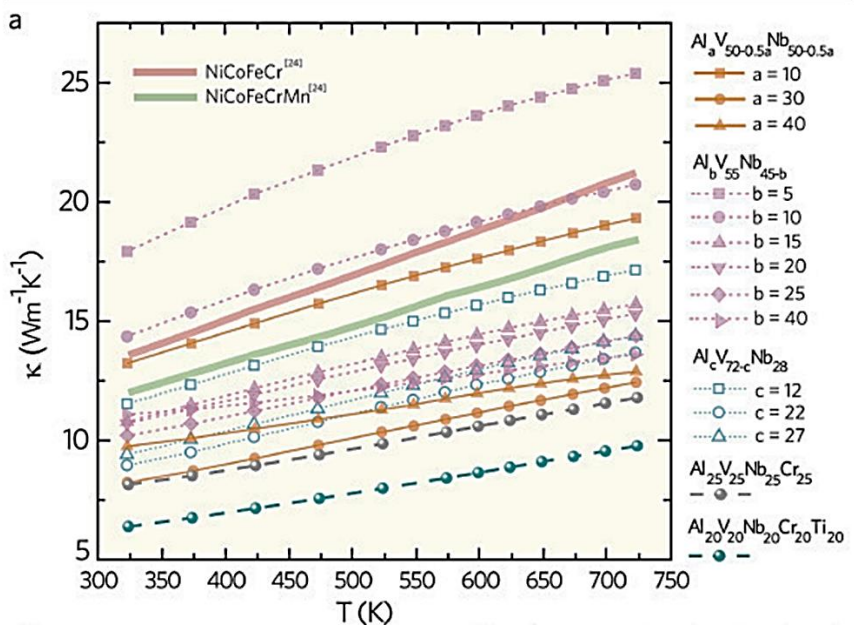

Fig. 1.10 Temperature-dependent thermal conductivity κ(T) for three series of ternary alloys with nominal compositions of $Al_aV_{50–0.5a}Nb_{50–0.5a}$ (a = 10, 30, 40), $Al_bV_{55}Nb_{45-b}$ (b = 5, 10, 15, 20,25, 40), $Al_cV_{72-c}Nb_{28}$ (c = 12, 22, 27), $Al_{25}V_{25}Nb_{25}Cr_{25}$, $Al_{20}V_{20}Nb_{20}Cr_{20}Ti_{20}$, NiCoFeCr and the NiCoFeCrMn.

1.7.3 Irradiation resistance

Nowadays, the irradiation resistance of austenitic stainless steel is often widely considered. Only a handful of irradiation studies have been conducted on HEAs, most of which are CoCrFeMnNi-type high-entropy alloys. The highly reduced diffusivity and deformed lattice in HEAs, which could immobilize the irradiation-induced point defects and prevent the clustering of defects, are believed to contribute to an improvement in the irradiation resistance of these materials.

Unlike FCC HEAs, there are few literatures related with irradiation resistance. As mentioned above, Nb-Ti-Zr is a successful BCC HEA system. Figure 1.11 compares the irradiation hardening of HfTaTiVZr and 304 stainless steels (SS304). The results indicate both the HEA and SS304 showed hardening after irradiation for the entire depth range of nano-indentation measurement. At the same time, the irradiation hardening for

HEA was considerably less than for SS304. The insets display hardness values for the depth range of 1500 nm–2000 nm, with HEA exhibiting 13% hardening compared to SS304's 50%. [59] The hardness of the irradiated sample did not approach that of the un-irradiated one at maximum depth because each indent sampled the entire region from the surface to the depth of indentation. [60] This study provides some evidence that BCC HEAs have better irradiation resistance than conventional alloys.

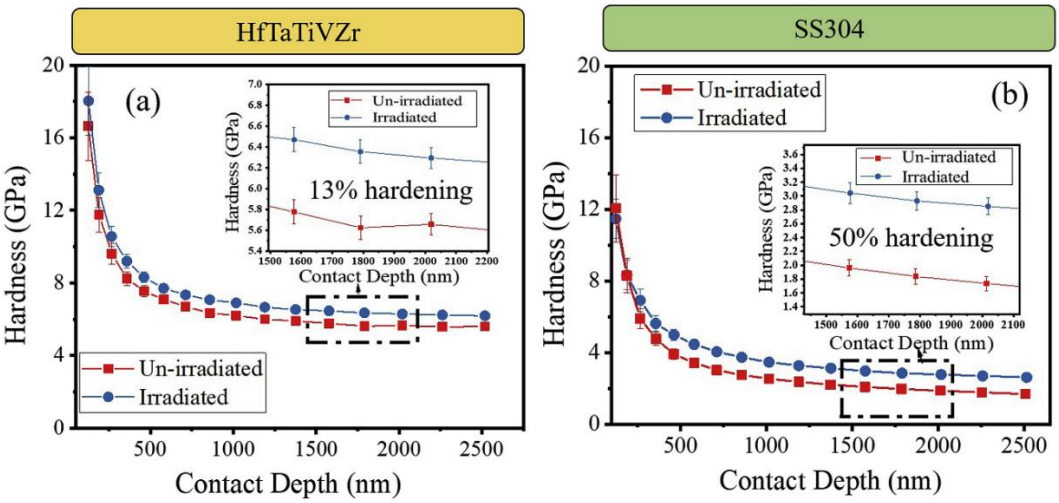

Fig. 1.11 Hardness versus depth for irradiated and un-irradiated samples of (a) HfTaTiVZr high entropy alloy and (b) 304 stainless steel (SS304).

1.8 Objective of this study

According to literature, refractory HEAs, which include several principal refractory elements (Zr, Ti, V, Hf, Ta, Nb, W, W, and Cr) has higher melting points at near-equiatomic concentrations. The refractory HEAs show superior high-temperature mechanical properties [61].

It is also known that several refractory elements suffer from low temperature embrittlement, while many refractory HEAs also possess limited ductility at room temperature. To enhance refractory HEA ductility, a series of BCC HEAs have been designed based on other elements Nb, Ta, and V, to form NbTaTiV, NbTaVW, NbTaTiVW, and MoNbTaV [62, 63].

Therefore, as high temperature structural materials, refractory metals own high melting points, superior performances in high temperature strength and ductility. It is expected that they can be applied to the systems as a functional conversion material with unexpected high performance. However, the research of HEAs seems to emphasize the alloys based on transition metals, there are few systematic efforts to explore refractory HEAs. Also, as for the irradiation effects on HEAs, there is only a limited study so many material issues of the irradiation effects still remain unknown. Therefore, in this research MoNbTaTi, MoNbTaW, MoNbTaTiW, HfNbTaTiZr and HfNbTaTiV high-entropy alloy was investigated with special focus on the irradiation hardening and microstructure.

Chapter 2

Experiment methodology

2.1 Vacuum melting

Arc melting and induction heating are generally utilized to produce alloys from different elements which require high-melting temperature, especially for arc-melting, inside temperature can reach more than 3000℃. The vacuum arc melting (VAM) process has revolutionized the specialty traditional metallurgical techniques industry and has made possible tightly controlled materials used in biomedical, aviation and aerospace. Comparing with traditional methods, VAM technique presents several advantages which include the solidification rate of molten material can be tightly controlled, centerline porosity and segregation are eliminated, elements with high vapor pressure such as carbon, sulfur, and magnesium (frequently contaminants) are lowered in concentration, and certain metals and alloys, such as Ti, cannot be melted in open air furnaces.

As shown in Figure 2.1, the melting process is through an electrical arc between tungsten electrode and metals placed in a crucible in a copper core. During the melting process, the chamber is evacuated and filled with argon gas. Since Ar is an inert gas that does not react with molten metal, the evacuation of the chamber prevents the oxidation of the melt alloys.

In this study, to fabricate body-centered cubic high-entropy alloys, pure W, Ti, Mo, Ta, Ti, V, Hf, Zr (>99.9 percent purity) were used as raw elements material. All HEAs (MoNbTaTi, MoNbTaW, MoNbTaTiW, HfNbTaTiZr and HfNbTaTiV) were made by arc-melting under a high vacuum, with the buttons turned and heated more than four times to achieve complete melting of all specimens.

Figure 2.1 Arc melting furnace with an enclosed crucible

2.2 X-ray fluorescence (XRF) spectrometry

XRF (X-ray fluorescence) is a non-destructive analytical technique used to determine the elemental composition of materials. XRF analyzers determine the chemistry of a sample by measuring the fluorescent (or secondary) X-ray emitted from a sample when it is excited by a primary X-ray source. The applications for XRF in industries include mining & exploration, oil and gas, metal fabricating, automotive & aerospace, precious metal recycling, construction & environmental engineering, and so on.

There are two main XRF methodologies: Energy Dispersive XRF (EDXRF) and Wavelength Dispersive XRF (WDXRF). In EDXRF spectrometers, the X-ray tube serving as a source directly irradiates the sample and the fluorescence from the sample is determined by an energy dispersion. When an atom in the sample is struck with an X-ray of sufficient energy, an electron from one of the atom's inner orbital shells is dislodged. The atom regains stability, filling the vacancy left in the inner orbital shell with an electron from one of the atom's higher energy orbital shells. The electron drops to the lower energy state by releasing a fluorescent X-ray. The energy of this X-ray is equal to the specific difference in energy between two quantum states of the electron. The measurement of this energy is the basis of XRF analysis

2.3 X-ray diffraction

There are many analytical issues related to the crystalline construction of material samples during the research process. XRD is a nondestructive technique which have many functions such as: 1) identifying crystalline phases and orientation, 2) determining structural properties: lattice parameters (10-4Å), strain, grain size, expitaxy, phase composition, preferred orientation, order-disorder transformation, and thermal expansion, 3) measuring thickness of thin films and multi-layers 4)determine atomic arrangement 4) Detection limits: ~3% in a two phase mixture; can be ~0.1% with synchrotron radiation.

In this research, the crystal structure of the annealed specimens was determined by X-ray diffraction (SmartLab XRD) with Cu K radiation at a speed of 6°/min.

Figure 2.2 The figure of SmartLab XRD

2.4 Scanning electron microscopy

A scanning electron microscope (SEM) is a type of electron microscope that produces images of a sample by scanning the surface with a focused beam of electrons. This analysis technique is utilized to test a material's microstructure, chemical distribution, and surface morphology. Because of the small beam, SEM micrographs have a broad depth of field giving a typical three-dimensional appearance that is useful for comprehending the surface structure of the sample. [64] Signals within SEM to create the picture is related with electron beam that encounter atoms at different depth of the sample. There are many types of signals including secondary electrons (SEs), characteristic X-rays and lights (CLs), backscattered electrons (BSEs), absorbed currents and transmitted electrons. Energy Dispersive spectroscopy (EDS) could be equipped with SEM to detect the microstructure. SEI and BEC images are obtained by the program to do the analysis.

For the BCC HEAs in this research, the samples were studied using a scanning electron microscope (SEM, JSM-6510LA) equipped with a 15 kV accelerating voltage energy dispersive spectrometer (EDS).

2.5 Vickers hardness

The Vickers hardness test was firstly developed by Robert L. Smith and George E. Sandland in 1921 at Vickers Ltd. to measure the hardness of materials [65]. The basic principle of Vickers hardness test is to observe a material's ability to resist plastic deformation from a standard source. The Vickers test can be utilized in all metals testing and has one of the widest applications among hardness tests. The unit of hardness of this test is known as the Vickers Pyramid Number (HV).

The HV number is then determined by the ratio F/A, and the F is the force applied to the diamond in kilograms-force and A is the surface area of the resulting indentation. A can be determined by the formula.

$$\mathrm{A} = \frac{d^2}{2\sin(136^o/2)} \qquad \text{(eq. 2-2)}$$

If d is the average length of the diagonal left by the indenter, the HV can be calculated as follows:

$$\mathrm{HV} = \frac{F}{A} \approx \frac{1.8544F}{d^2}\ [kgf/mm^2] \qquad \text{(eq. 2-3)}$$

In this study, Vickers micro-hardness was measured on polished cross-section surfaces using a Vickers diamond pyramid under 9.87 N load and room temperature applied for 15s.

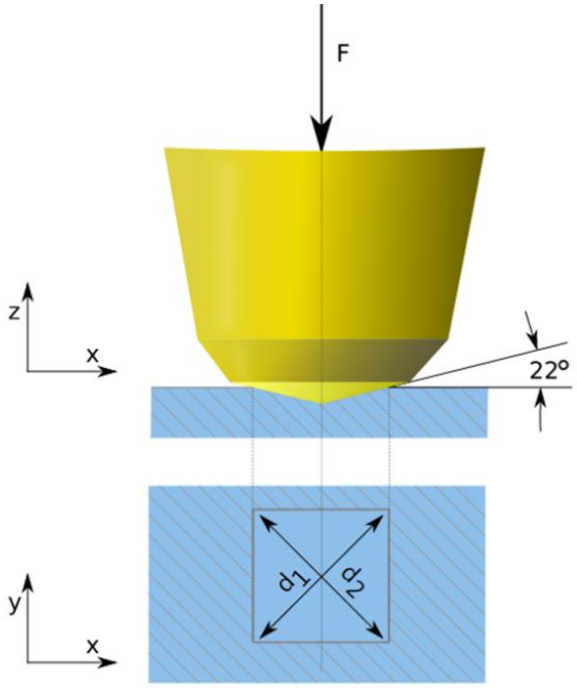

Fig. 2.3 Vickers test scheme

2.6 Ion-irradiation experiments

In general, ion irradiation relates using particle accelerators to fire energetic ions through a substance. As particle accelerators rapidly irradiate heavy ions with radiation, ion tracks are produced that can be utilized in nanotechnology.

In this study, three refractory high-entropy alloys, MoNbTaTi, MoNbTaW, and MoNbTaTiW, were irradiated at Kyoto University's dual-beam irradiation experimental test facility (DuET). Three HEAs were irradiated with 6.4 MeV Fe^{3+} ions at a concentration of 3.06 × 10^{19} ions/m^2 at a flux of 8.50 × 10^{15} ions/m^2/s and at a temperature of 500°C. The BCC HEAs HfNbTaTiV F82H and HfNbTaTiZr (Senkov alloy) were also irradiated DuET and irradiated with 6.4 MeV Fe^{3+} ions at 300 °C for 5h. The depth profile of damage and the concentration of implanted elements, which were simulated by SRIM software. Stopping and Range of Ions in Matter (SRIM) is a group of computer programs. It calculates interaction of ions with matter and the Transport of ions in matter (TRIM) is the core of SRIM program. SRIM is mostly applied in the ion implantation technology and research community and used in other fields of radiation material science. The programs were introduced by James F. Ziegler and Jochen P. Biersack around 1983 [66, 67]. SRIM is based on a Monte Carlo simulation method, which is also called binary collision approximation [68, 69] with a random selection of the impact parameter of the next colliding ion.

Fig. 2.4 The picture of Dual-Beam Facility for Energy Science and Technology (DuET)

Fig. 2.5 The holder for irradiation specimen

2.7 Nanoindentation

Nano-indentation was tested by G200 Agilent Tech with a Berkovich tip. Continuous stiffness measurement (CSM) method was applied with the area function (equation 2.2) calibrated on standard fused silica by Oliver and Pharr [70]. The strain rate was 0.05 /s and the oscillations set as 2 nm. The maximum penetrating depth was 2000 nm. Testing temperature was controlled to 25 ± 4°C. The selection of zero point followed the rule that within 0~5nm, for which the contrast stiffness should show significant increasing trend. This means the tip could solidly contact with the surface of the specimen. The area-function (A), for an ideal Berkovich tip, is defined as A = 24.56 h^2, and h is indentation depth. The tip blunting that alters h should be considered because the nano-indentation hardness is affected by A.

$$A = 24.5h_c^2 + C_1h_c^1 + C_2h_2^{1/2} + \cdots + C_8h_c^{1/128} \qquad \text{(eq. 2-4)}$$

The CSM technique can be used to continuously obtain hardness and elastic modulus data along the entire applied loading schedule, and the stiffness S of the instantaneous tip–sample contact can be calculated as:

$$\frac{1}{S} = \frac{1}{\left(\frac{P_o}{h_0}\right)\cos\emptyset - (K_s - m\omega^2)} - \frac{1}{K_f} \qquad \text{(eq. 2-5)}$$

P_o: the amplitude

ω: the frequency

∅: the phase angle between the force and displacement of the indenter

K_S:the constant of the springs supporting the indenter

K_f: the stiffness of the indenter frame

m: the mass of the indenter

Fig 2.6 the picture of Nanoindenter G200

2.8 Transmission electron microscope (TEM)

Transmission electron microscopy (TEM) is a microscopy technique in which a beam of electrons is transmitted through a specimen to form an image. The specimen is most often an ultrathin section less than 100 nm thick or a suspension on a grid. Comparing with SEM, which can only provide details on the morphology pf the specimen, TEM can give us the details about a specimen's structure, morphology, crystallization, and stress.

TEM are capable of imaging at a significantly higher resolution than light microscopes, owing to the smaller de Broglie wavelength of electrons. This enables the instrument to capture fine detail—even as small as a single column of atoms, which is thousands of times smaller than a resolvable object seen in a light microscope. Transmission electron microscopy is a major analytical method in the physical, chemical and biological sciences. TEMs find application in cancer research, virology, and materials science as well as pollution, nanotechnology and semiconductor research, but also in other fields such as paleontology and palynology.

Within this research, TEM images and diffraction patterns were obtained using a JEOL 2010F operated at 200 kV. The defect cluster data after irradiation were obtained by removing the data at around 2.5 m from the surface while accounting for FIB irradiation damage.

Chapter 3

Study on irradiation effects of refractory bcc high-entropy alloy

3.1 Introduction

As is well known, conventional alloys contain the primary element, comprising around 80% to 90% of the alloy composition. Even superalloys, which contain 12 elements, also contain a minimum of 50% of the primary elements. [24] Researchers have recently proposed high entropy alloys (HEA), which have garnered considerable attention as potential material. According to Yeh's composition-defined definition, HEAs comprise four or more elements in equimolar or near-equimolar proportions, with element concentrations ranging from 5% to 35%. [71,72,28] The entropy-based definition defines the HEA as having the highest potential entropy, implying that such a state is achievable at extremely high temperatures or in the liquid form. Researchers hypothesized that HEAs had a complex element composition, but a simple structure based on their high-entropy effect. Additionally, it has been demonstrated that certain HEAs exhibit excellent mechanical properties from cryogenic to high temperatures. [73-75]

The materials applied in fusion reactors are subjected to tremendous heat flow and high-energy particles, necessitating materials with excellent thermal conductivity and irradiation resistance. According to the literature, candidates for fusion reactor refractory metals include Ta and Mo alloys due to their superior high-temperature strength and ductility. [61] Additionally, W has attracted significant emphasis as an ideal material for in-vessel components such as diverters and blankets in a fusion reactor because of its high-temperature capabilities and low sputtering yield. However, tungsten's inherent brittleness at low temperatures and irradiation embrittlement have precluded its usage in fusion reactor applications. [62,63] Considering this, some investigations have focused on using HEAs in place of tungsten. Because the ductility of the Ti element is more significant than that of the refractory components (W, Ta). Ti was added to the HEAs to improve their properties. Corrosion resistance is required for the material used in fusion reactors. Although Mo and Nb are not low activation elements, they are typical elements that improve the corrosion resistance of stainless

steel and other superalloys. [76-79] Therefore, refractory HEAs (which contain Ti, Zr, Hf, Ta, V, Nb, W, and Cr) are one type of contender because they display exceptionally high melting points, ductility, and strength at elevated temperatures. The microstructure and irradiation hardening of three HEAs (MoNbTaTi, MoNbTaW, and MoNbTaTiW) were examined in this work as part of the development of HEAs suitable for fusion reactors.

3.2 Fabrication of refractory high-entropy alloys (MoNbTaTi, MoNbTaW, and MoNbTaTiW)

To fabricate three body-centered cubic high-entropy alloys, pure tungsten, niobium, titanium, tantalum, and molybdenum (>99.9 percent purity) were used as raw elements material. All HEAs (MoNbTaTi, MoNbTaW, and MoNbTaTiW) were made by arc-melting under a high vacuum, with the buttons turned and heated more than four times to achieve complete melting of all specimens.

Table 3.1 contains the chemical compositions of the three alloys found using an ED-XRF (Energy Dispersive X-Ray Fluorescence) spectrometer. All ingots were solution-annealed at 1200°C to achieve homogeneously. The phase diagrams were calculated in Fig 3.1 with the CALPHAD methodology. CALPHAD methodology is a phenomenological approach for calculating/predicting thermodynamic, kinetic, and other properties of multicomponent materials systems. [80] Because MoNbTaW has a higher melting point than the other two HEAs, 1500°C annealing is also used. Table 3.2 contains the solution annealing conditions for the three alloys.

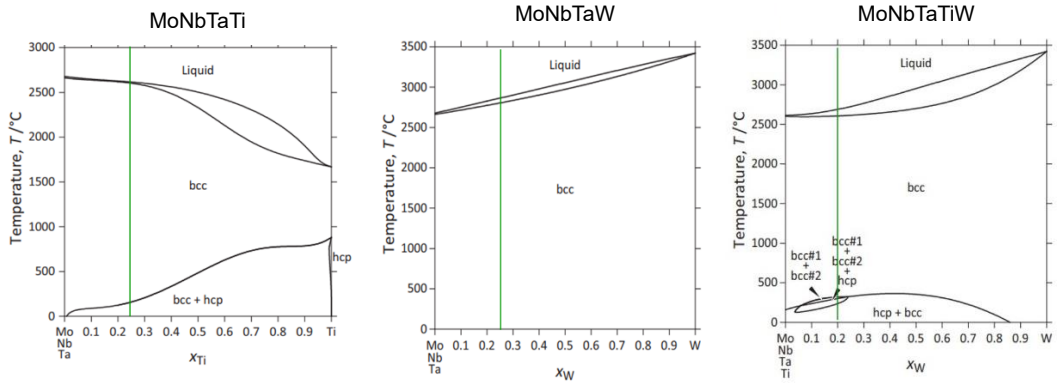

Fig. 3.1 Phase diagram for three refractory HEAs.

Table 3.1. Chemical composition of MoNbTaW, MoNbTaTi, MoNbTaTiW produced by vacuum arc melting tested with XRF

at(%)	**W**	**Nb**	**Ta**	**Ti**	**Mo**
MoNbTaTi	-	21.88	28.17	25.52	25.15
MoNbTaW	25.57	23.21	27.45	-	25.57
MoNbTaTiW	17.87	23.11	18.80	17.24	22.98

The microstructures of the alloys were studied using a scanning electron microscope (SEM, JSM-6510LA) equipped with a 15 kV accelerating voltage energy dispersive spectrometer (EDS). The crystal structure of the annealed specimens was determined by X-ray diffraction (SmartLab XRD) with Cu K radiation at a speed of 6°/min. The hardness of the samples was determined at room temperature using a Vickers indenter (Struers) with a force of 1 kg and a dwell period of 15 s.

The specimens were irradiated at Kyoto University's dual-beam irradiation experimental test facility (DuET). Three HEAs were irradiated with 6.4 MeV Fe^{3+} ions at a concentration of 3.06 × 10^{19} ions/m2 at a flux of 8.50 × 10^{15} ions/m^2/s and at a temperature of 500°C. The depth profile of displacement damage calculated using the stopping and range of ions in the matter (SRIM) package is depicted in Figure 2. [68,81,82] To investigate the performance of irradiation hardening, a nano-indentation test was conducted using a nanoindenter (Agilent Technologies Inc. Model Nano Indenter G200) with a Berkovich-type indentation tip. Moreover, indentation was performed on the irradiation surface in the direction parallel to the incident Fe^{3+} beam. The constant stiffness measurement (CSM) technique was used to obtain the depth profile of the hardness [83].

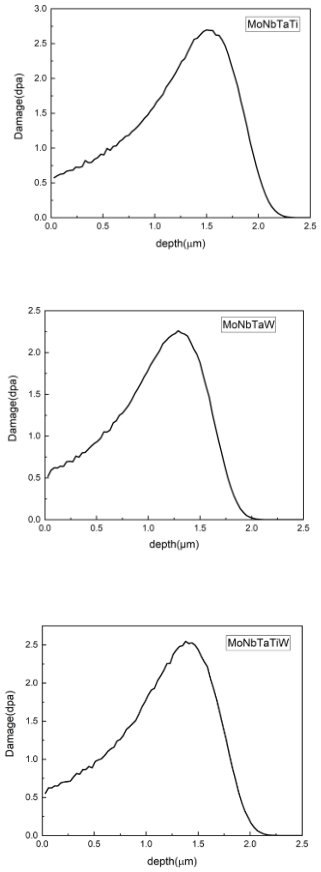

Fig. 3.2 Depth profile of damage induced by irradiation with 6.4 MeV Fe^{3+}

Table 3.2. Solution annealing conditions of refractory bcc high-entropy alloys

	Heat treatment condition
MoNbTaW (A-W)	1200℃/48h and 1500℃/48h
MoNbTaTi (A-Ti)	1200℃/48h
MoNbTaWTi (A-WTi)	1200℃/48h

3.3 Analysis of the microstructure

Table 3.1 contains the chemical compositions of the three alloys with XRF, and the results indicate that all the as-cast alloys are close to homogeneous. According to Figure 3.1, the phase diagram shows MoNbTaTi (A-Ti) and MoNbTaW (A-W) are single BCC alloys from room temperature to the melting point. In contrast, the phase diagram for MoNbTaTiW(A-TiW) is unstable from room temperature to 400°C with bcc and hcp phases.

Figure 3.4 shows Typical SEM-BEC images of as-cast alloys and indicates no contrast in all three alloys. However, the EDS mapping result for as-cast A-TiW (Fig. 3.5) indicates that the material consists of two phases, each of which contains five elements. This EDS mapping result is constituent with the phase diagram mentioned above. Therefore, high-temperature heat treatment is required for refractory HEAs. Three HEAs become single-phase alloys following heat treatment at 1200°C; the phase results are also evaluated using XRD. The diffraction peaks of MoNbTaTi, MoNbTaW, and MoNbTaTiW after annealing are shown in Figure 3.3. The diffraction peaks of three HEAs were identical to those of the single-phase BCC alloys.

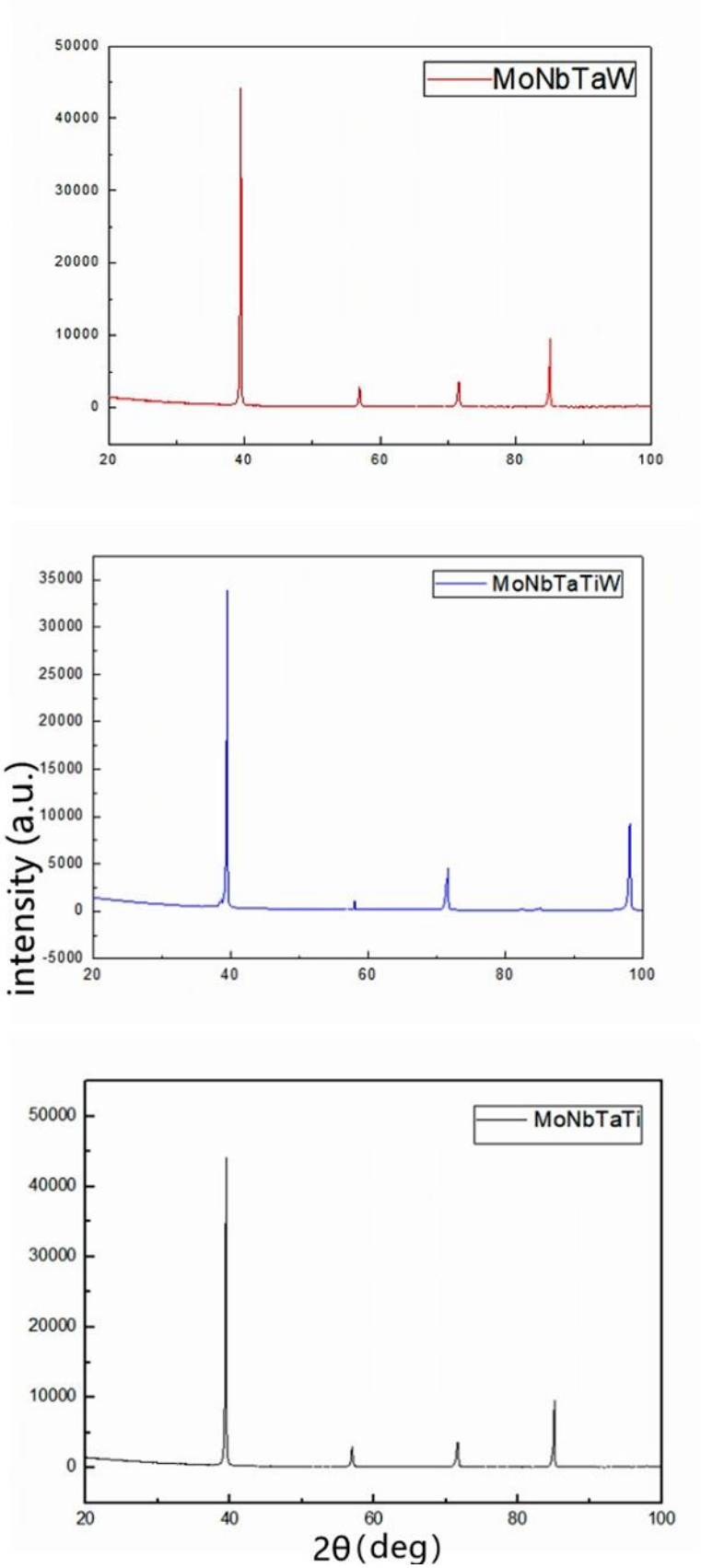

Fig.3.3 XRD patterns for the three high-entropy alloys after heat-treatment

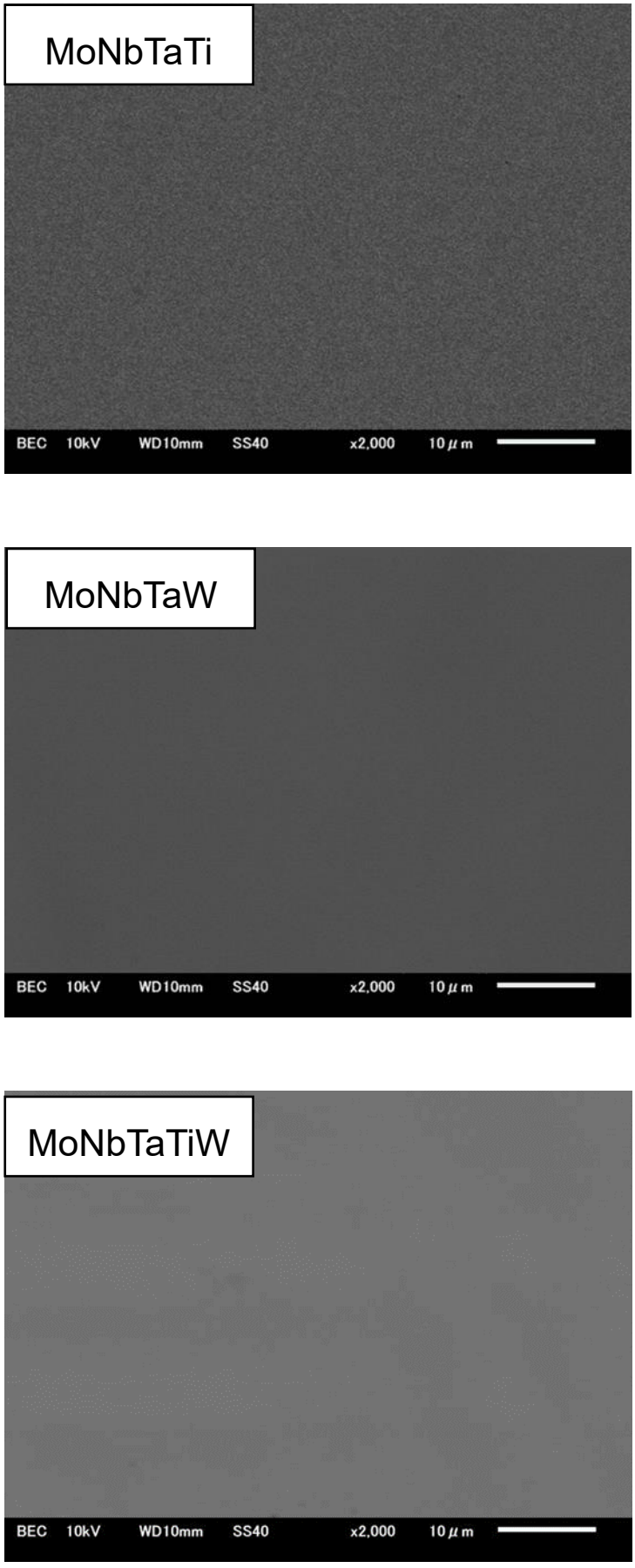

Fig. 3.4 Typical SEM-BEC images of as-cast alloys.

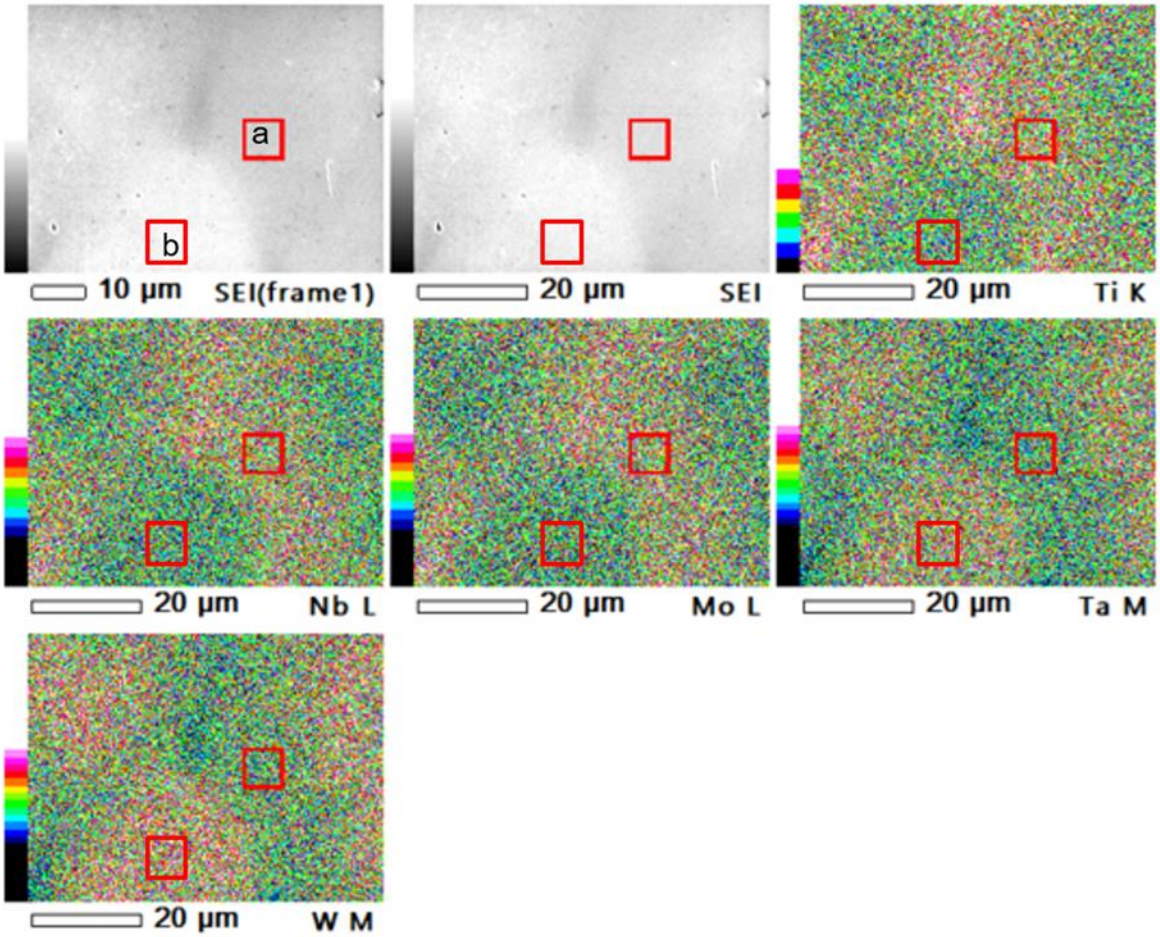

Fig. 3.5 EDS-mapping image of MoNbTaTiW.

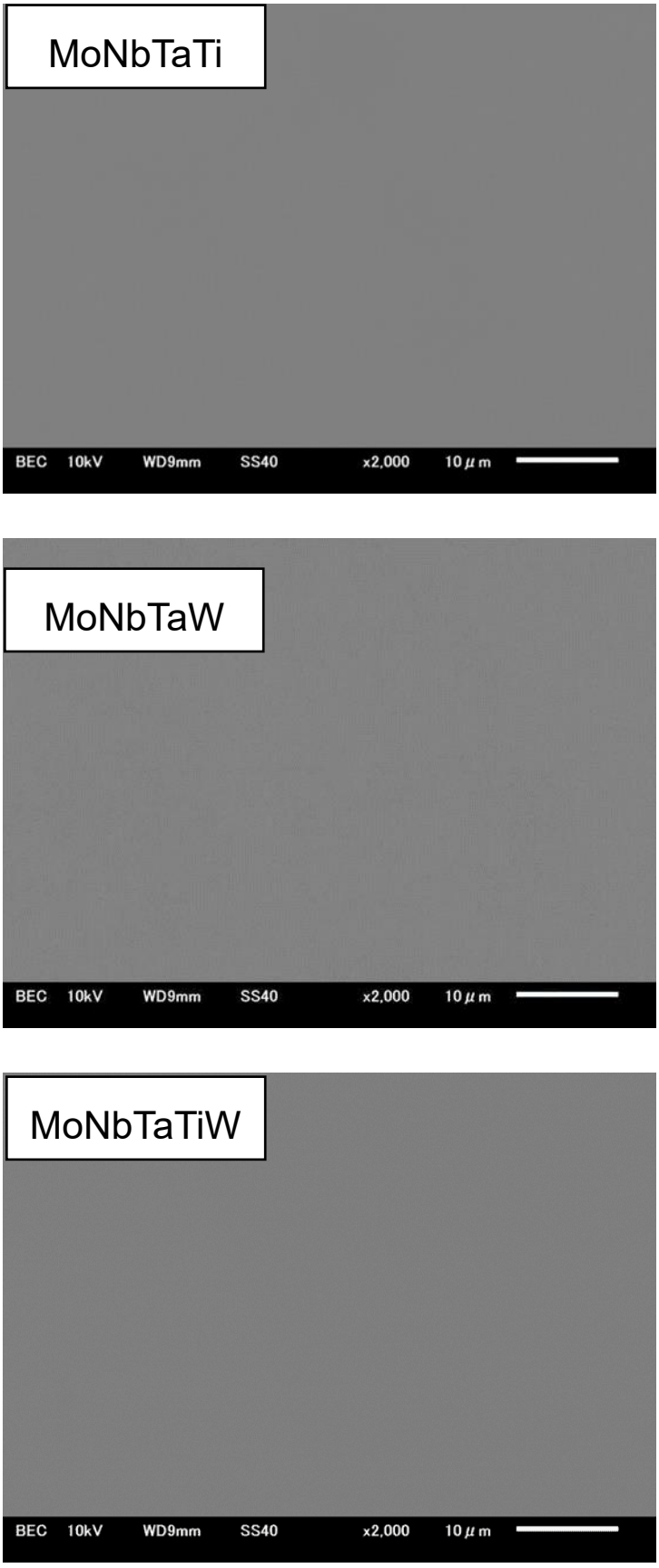

Fig. 3.6 Typical SEM-BEC images of annealed alloys (1200℃, 48h).

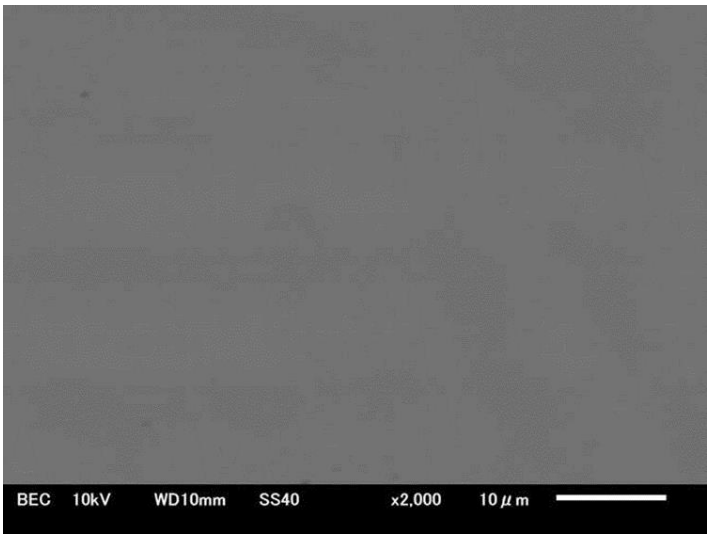

Fig. 3.7 Typical SEM-BEC images of MoNbTaW after 1500℃, 48h heat-treatment

As indicated in Figures 3.6 and 3.7, the BEC pictures for three refractory HEAs after 1200℃ annealing or 1500℃ annealing also demonstrate its high-temperature stability, as no phase shift occurs during annealing. Compared with other conventional alloys, this microstructure study indicated that high-entropy alloys had a simple microstructure despite their complex element constituents.

3.4 Vickers hardness

Vickers hardness values for three HEAs are shown in Figure 3.8 before and after annealing. Vickers hardness values for annealed alloys were nearly identical to those for as-cast alloys. While A-W has a higher hardness than A-Ti and A-TiW, this is due to the higher hardness of pure tungsten in comparison to pure titanium. Additionally, the hardness of A-TiW is greater than that of A-Ti; this is owing to the typical hardening effect of solid solutions. It should be noted that the hardness of three HEAs was significantly higher (A-W: 550 Hv, A-Ti: 420 Hv, and A-TiW: 479 Hv) than that of pure tungsten (260-320 HV), which would be used for the International Thermonuclear Experimental Reactor's high heat flux components (ITER).

Fig. 3.8 Vickers hardness of all the alloys of as-cast and solution annealed for 48h.

3.5 The result of nano-indentation

Fig. 3.9 illustrates the indentation depth profiles of three HEAs in the direction parallel to the incoming Fe^{3+} beam before and after ion irradiation, matching their nano-indentation hardness. The indentation size effect was found for all specimens, and the assessed hardness decreased with increasing indentation depth. Hardness fluctuations occurred at a depth of 400 nm in irradiated specimens, showing that the region of indentation-induced deformation extended to the boundary between the irradiated and unirradiated regions. Fig 3.10 illustrates the Nix-Gao model for three HEAs, demonstrating that A-Ti and A-TiW exhibit evident irradiation hardening, whereas A-TiW exhibits less irradiation hardening than A-Ti. This could be related to the high-entropy effect, which states that increasing entropy can stabilize a phase with a greater entropy at elevated temperatures. Because the nano-indentation result is unreliable below 100nm, the nano-indentation hardness at 350 nm was used to compare the pre- and post-irradiation stages.

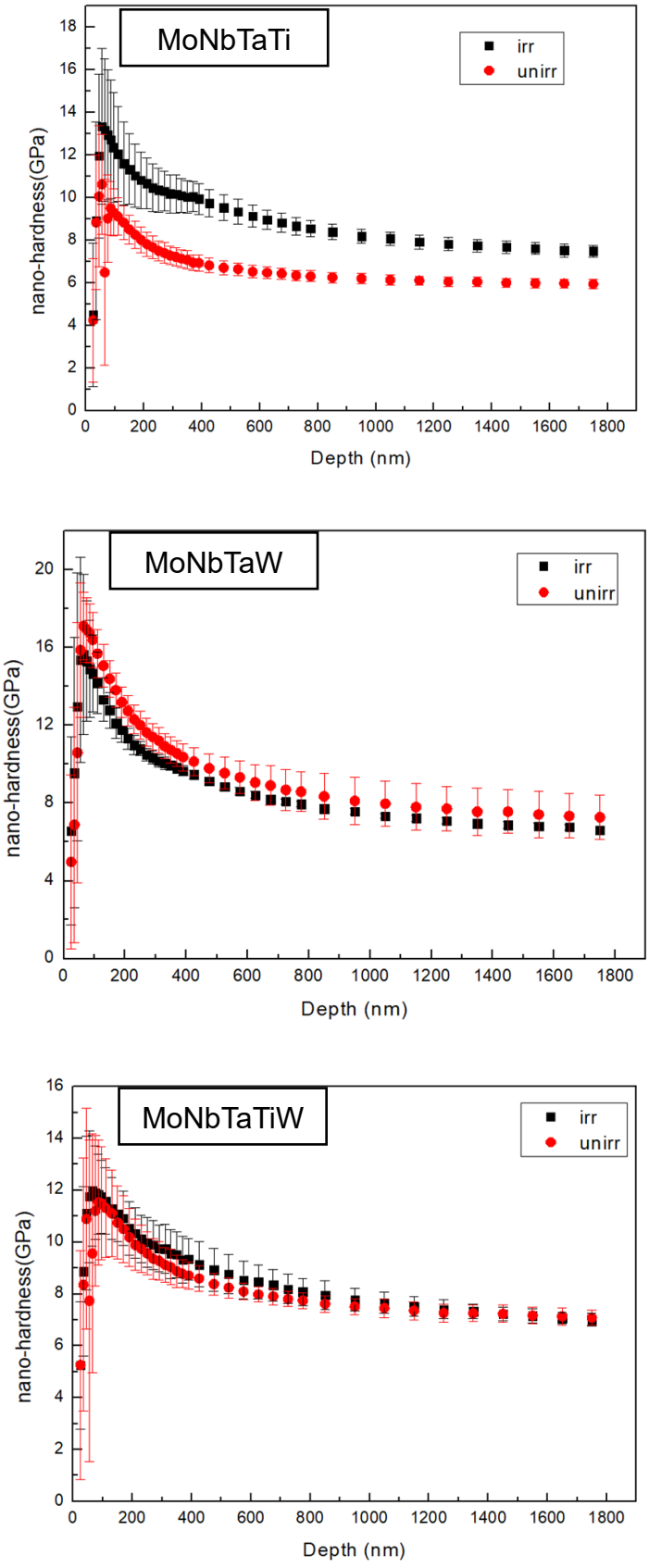

Fig. 3.9 Depth profiles of nanohardness in the direction parallel to the incident Fe^{3+} beam before and after ion irradiation

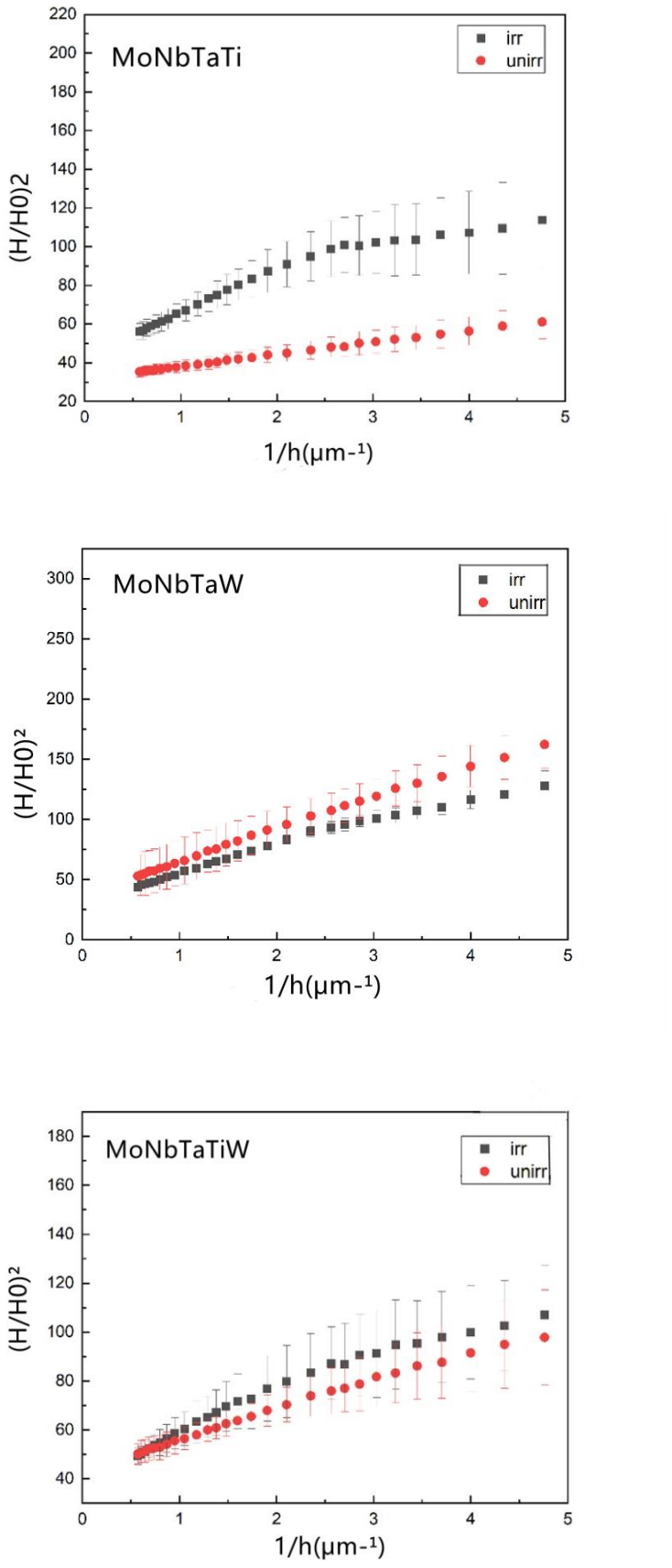

Fig. 3.10 Nix-Gao model for three HEAs after ion irradiation.

Fig. 3.11 illustrates the results of irradiation hardening on the alloy and recrystallized pure W [84], both of which were irradiated with 6.4 MeV Fe^{3+} ions at the same ion irradiation facility (DuET). Zhang et al. explored irradiation hardening using a Nix–Gao equation-based approach. The nano-indentation hardness at 350 nm was chosen for comparison with our findings, and the irradiation hardening was displayed. Fig. 3.11 demonstrates that the irradiation hardening of three HEAs is less than that of pure tungsten, implying that refractory BCC HEAs are more resistant to irradiation than pure tungsten. Besides the high-entropy effect, the high-entropy alloys also have the cocktail effect; their properties are certainly related to the properties of their compositing elements, which may also increase their mechanical properties, high-temperature behavior, and irradiation resistance.

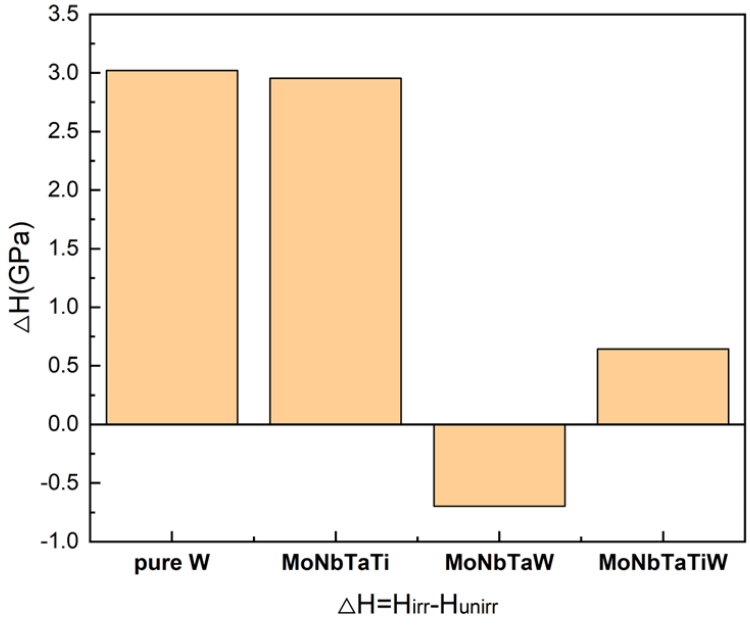

Fig. 3.11 Irradiation hardening of three BCC HEAs irradiated at 500℃ and compare with pure W

3.6. Summary

Refractory high-entropy alloys: MoNbTaW, MoNbTaTi, MoNbTaTiW were produced by vacuum arc melting with pure metals and irradiated by DUET with 6.4 MeV Fe^{3+} at 500℃.

After heat treatment at 1200°C or 1500°C, the three HEAs transformed into single-phase bcc alloys. The average Vickers hardness of three alloys was almost the same after annealing at 1500°C or 1200°C, indicating that they exhibit high-temperature stability (MoNbTaW: 550 Hv, MoNbTaTi: 420 Hv, MoNbTaTiW: 479 Hv). From the Nix-Gao model result, the irradiation hardening of MoNbTaTiW is less than that of MoNbTaTi, possibly because of the high entropy effect. There is no noticeable irradiation hardening of MoNbTaW. At a depth of 350nm, the irradiation hardening of MoNbTaTi and MoNbTaTiW was less than that of pure W. (peak region). Additional TEM observations of irradiated specimens and analysis of the nano-indentation result and TEM image will be required.

Chapter 4

Irradiation behavior of HfNbTaTiV in comparison of HfNbTaTiZr and F82H

4.1 Introduction

A typical high-entropy alloy is the CoCrFeMnNi alloy, which consists of five elements and is commonly referred to as Cantor alloy [18]. This alloy consists of a single fcc solid solution and possesses great thermomechanical stability [85] and superior ductility [86]. Particularly, its low-temperature ductility and tensile strength make it a viable structural material. HfNbTaTiZr (Senkov alloy) is another high-entropy alloy made of a single bcc solid solution. It is also known as the first high-entropy alloy with a BCC crystal structure that was successfully cold-rolled [87] and possesses significant ductility in BCC-type HEA.

Materials utilized in fusion reactors are subjected to extreme heat flow and high-energy particles, necessitating materials with superior thermal conductivity and radiation resistance. Due to their high-temperature capabilities and low sputtering yield as bcc alloys, metals including Ta and Mo, as well as pure W, have garnered substantial attention as excellent materials for in-vessel components such as diverters and blankets in a fusion reactor [61].

In light of this, we wish to study a bcc high-entropy alloy that can be utilized in a fusion reactor [62,63,88]. As previously stated, many BCC alloys are very brittle. To manufacture the bcc high-entropy alloy with greater ductility, we studied the manufacturing of alloys derived from the Senkov alloy. According to the phase diagram, alloys devoid of Ti have a two-phase structure following heat treatment. Therefore, adding Ti to our bcc high-entropy alloy is required. Because the inclusion of Cr, Mo, and W frequently causes embrittlement in BCC high-entropy alloys, we determined to add V to the BCC high-entropy alloys in this study. In this study, the mechanical properties and irradiation hardening of three HEAs (HfNbTaTiV, Senkov alloy, and F82H) were examined in order to develop HEAs that perform well in fusion reactors.

4.2 Fabrication of refractory high-entropy alloys (HfNbTaTiV and Senkov alloy)

To fabricate the body-centered cubic high-entropy alloys, the pure metallic elements V (99.9 %), Ti (99.9 %), Zr (99.9 %), Nb (99.9 %), Hf (99.9 %), and Ta (99.95 %) were utilized as raw materials and weighed using an electrical balance to a total of roughly 30 g. All HEAs (HfNbTaTiV and Senkov alloy) were manufactured by arc-melting under a high vacuum, with the buttons being rotated and heated more than ten times to ensure the full melting of all specimens.

The chemical compositions of the three alloys discovered with an X-ray fluorescence spectrometer are listed in Table 4.1. (XRF JEOL JSX3100RII). Table 4.2 demonstrates the heat-treatment condition. In Fig. 4.1, the phase diagram of HfNbTaTiV was calculated using the CALPHAD methodology. CALPHAD is a phenomenological method for calculating and forecasting thermodynamic, kinetic, and other properties of multicomponent material systems [80].

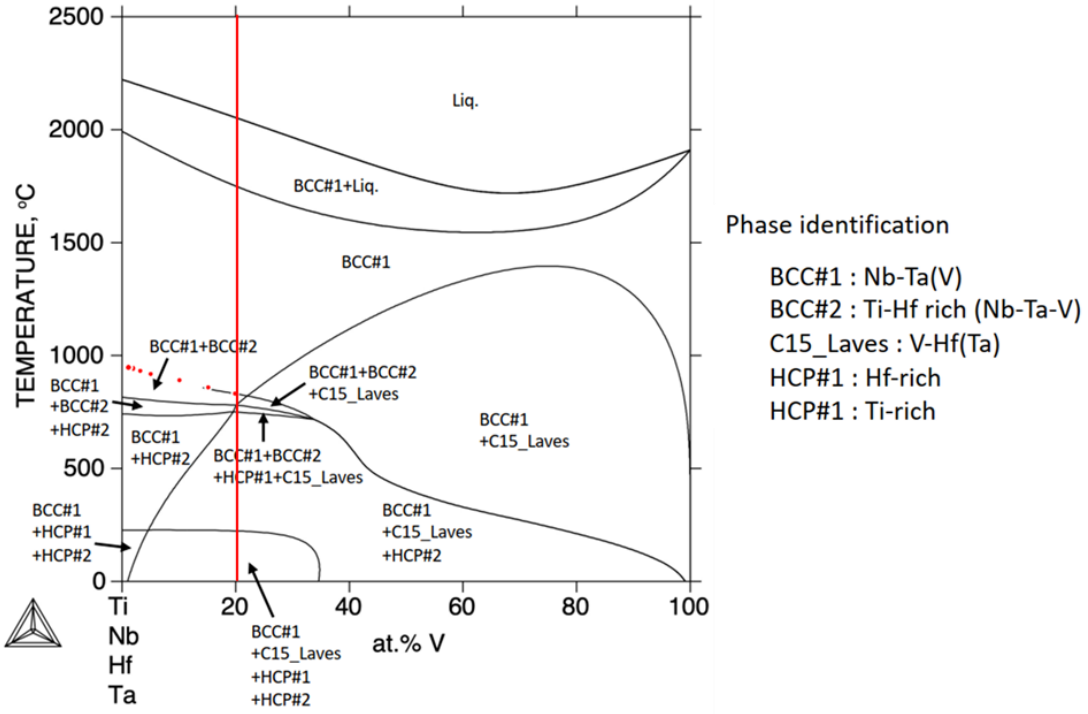

Fig. 4.1 Phase diagram for HfNbTaTiV

Table 4.1. Chemical composition of HfNbTaTiV and Senkov alloy produced by vacuum arc melting tested with XRF

		Ti	V	Zr	Nb	Hf	Ta
HfNbTaTiV	experimental	20.0	22.0		19.6	18.9	19.5
	theoretical	20.0	20.0		20.0	20.0	20.0
HfNbTaTiZr (Senkov alloy)	experimental	20.6		20.0	20.2	19.8	19.4
	theoretical	20.0		20.0	20.0	20.0	20.0

Table 4.2. Heat-treatment conditions of HfNbTaTiV, Senkov alloy, and F82H

	HfNbTaTiV, Senkov alloy	F82H
Temperature [℃]	1160	800
Time [min]	45	180

The microstructures of the alloys were investigated using a scanning electron microscope (SEM, JSM-6510LA). The crystal structure of the annealed specimens was determined by X-ray diffraction (SmartLab XRD) with Cu K radiation at a speed of 6°/min. Each sample was processed and cold rolled approximately 90% to a thickness of approximately 0.25 mm to investigate the presence of ductility. The average hardness of the samples was determined at room temperature using a Vickers indenter (Struers) with testing more than ten times.

The specimens were irradiated at Kyoto University's dual-beam irradiation experimental test facility (DuET). Three HEAs were irradiated with 6.4 MeV Fe^{3+} ions at 300 °C for 5h. The depth profile of displacement damage calculated using the stopping and range of ions in the matter (SRIM) package is depicted in Fig. 4.2. The Nano Indenter TI-950 (Hysitron) was used as the nanoindentation test device. In this study, the indentation depths were 100, 200, and 250 nm. At least 10 measurements were taken for each, and the average value was calculated. TEM observation was performed at an acceleration voltage of 200 keV to observe the microstructure after irradiation. The defect cluster data after irradiation were obtained by removing the data at around 2.5 m from the surface while accounting for FIB irradiation damage.

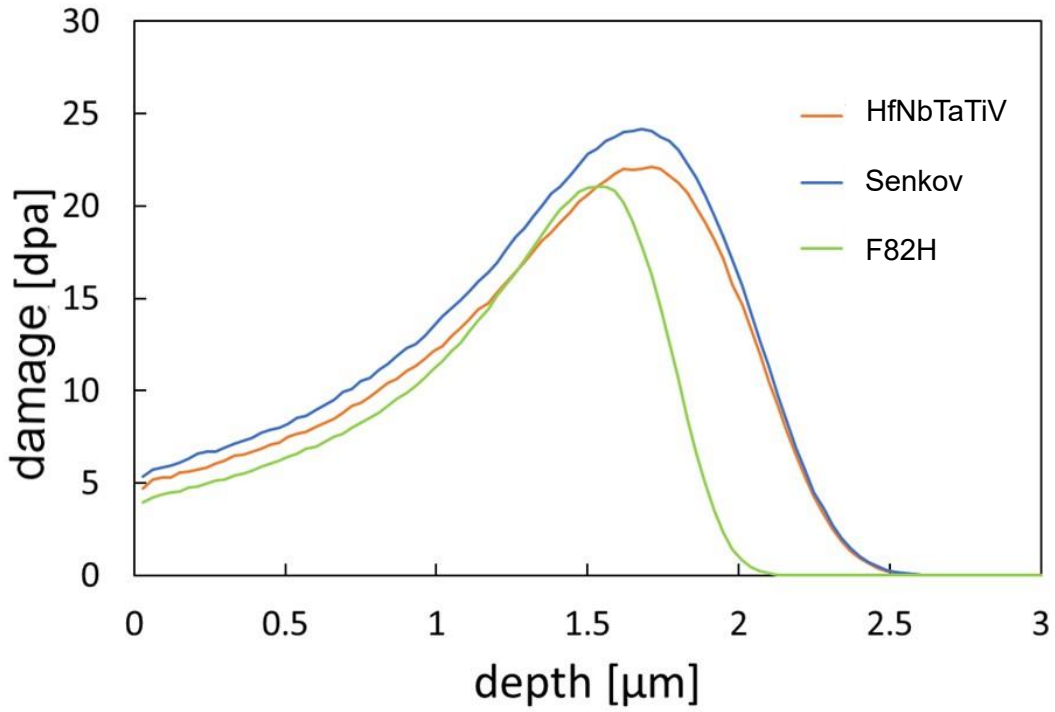

Fig. 4.2 Depth profile of displacement damage (dpa) induced by irradiation with 6.4 MeV Fe^{3+}.

4.3 Microstructure analysis

The refractory high-entropy alloys (HfNbTaTiV and Senkov alloy) were shown in Figs. 4.3 and 4.4 with their XRD diffraction profiles and reflection electron images both before and after homogenization heat treatment. A single peak of Nb with the BCC crystal structure was consistent with the HfNbTaTi results both before and after heat treatment. As seen in Fig. 4.3, HfNbTaTiV was initially found two-bcc matrix, but after homogenization heat treatment, it changed into a single-phase bcc alloy. Fig. 4.4 shows that the Senkov alloy has a BCC single-phase microstructure since no multiple phases were observed both after as-cast and homogenization heat treatment and the peaks were consistent with a BCC crystalline structure, ZrNb. In order to further investigate this phase, we performed a lattice parameter study and determined the theoretical values of the lattice parameters for each of the phases shown in Table 4.3. The theoretical values can be calculated with the equation:[89]

$$a = \sum a_i x_i \qquad (3.1)$$

where a_i is the lattice constant of element i, and x_i is the mole fraction of element i.

The theoretical values of each phase's lattice constants are nearly consistent with their XRD data. As a result, the two phases observed in Fig. 4.3 are believed to be two comparable BCC phases with very close lattice characteristics. According to the microstructure observations, HfNbTaTiV and Senkov alloy are stable with a single bcc phase after homogeneous heat-treatment and have the potential to be used in nuclear reactor environments.

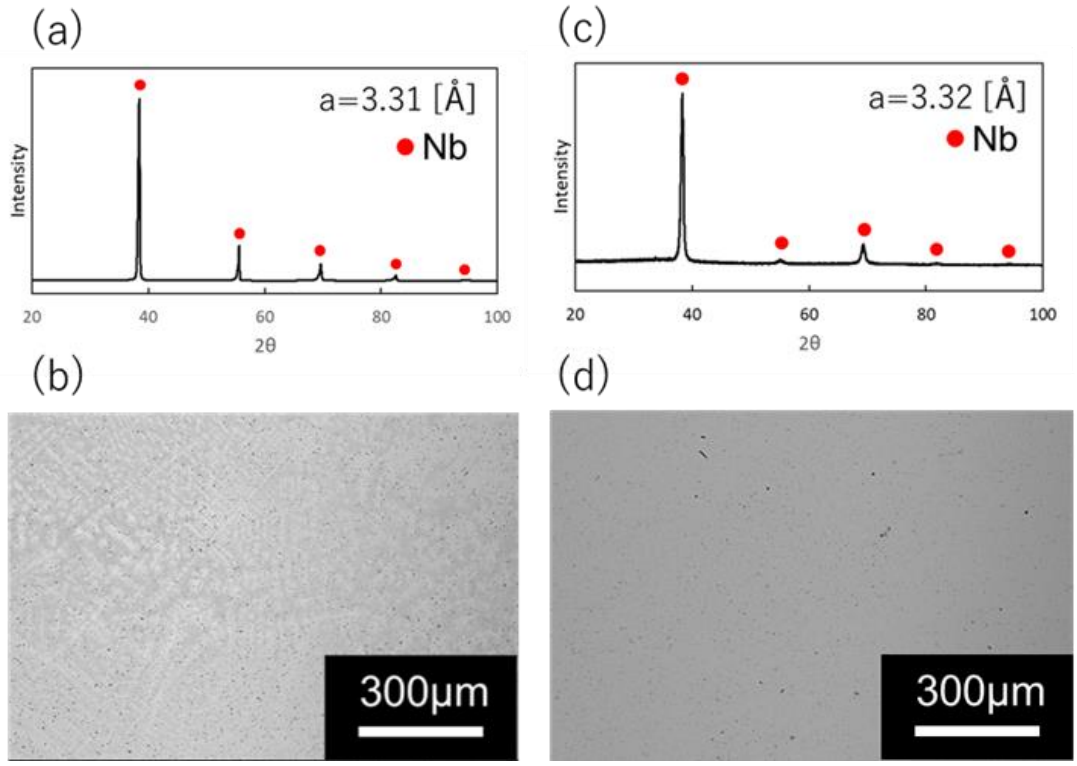

Fig. 4.3 The image of As-cast condition in HfNbTaTiV, (a) XRD diffraction peak and (b) reflection electron image, the image after homogenization heat treatment, (c) XRD diffraction peak and (d) reflection electron image.

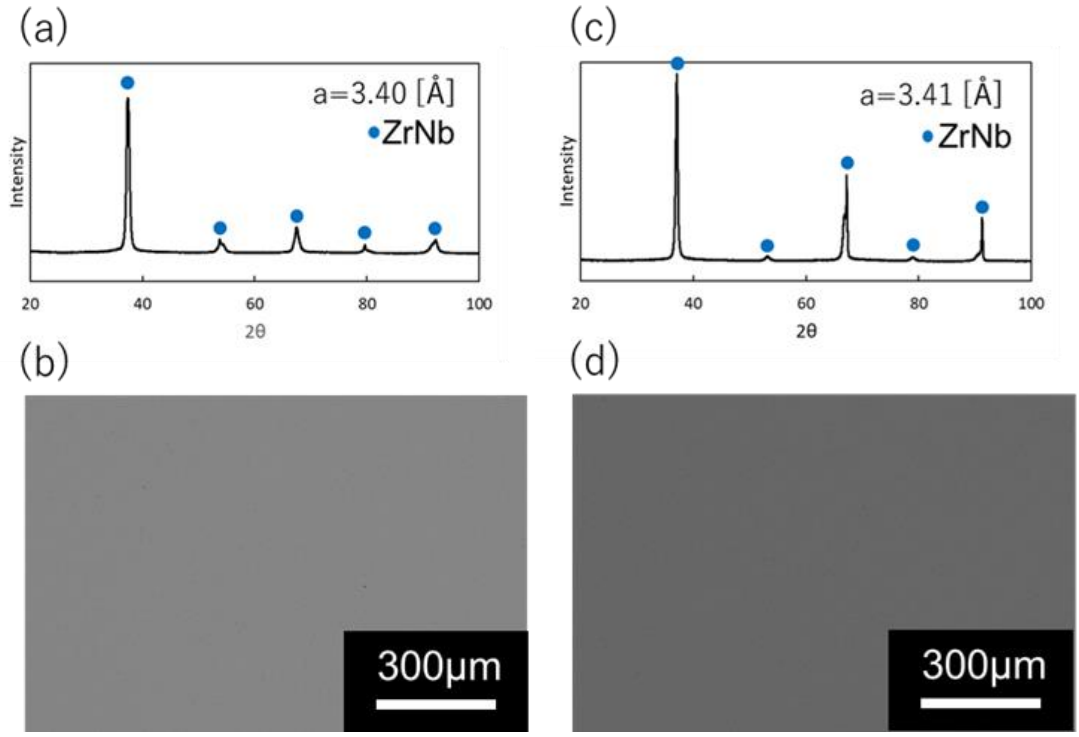

Fig. 4.4 The image of As-cast condition in senkov alloy, (a) XRD diffraction peak and (b) reflection electron image, the image after homogenization heat treatment, (c) XRD diffraction peak and (d) reflection electron image.

Table 4.3. Lattice parameter for pure element [21], HfNbTaTiV and Senkov alloy (Å)

Ti	V	Nb	Hf	Ta	HfNbTaTiV	Senkov alloy
3.276	3.095	3.301	3.559	3.303	3.32	3.41

4.4 Mechanical properties analysis

The Vickers hardness test results were shown in Fig. 4.5. The refractory high-entropy alloy had a higher Vickers hardness than the comparator sample, F82H. HfNbTaTiV has a higher Vickers hardness than Senkov alloy. The tensile test results were shown in Fig. 4.6. The order of yield stress was F82H, Senkov alloy, and HfNbTaTiV, and that the yield stress of HfNbTaTiV is around 1200 MPa. Elongation, on the other hand, was found to be greater in the order of HfNbTaTiV, Senkov alloy, and F82H.

High-entropy alloys are known to have high strength due to solid solution strengthening produced by the high concentration of atoms of different atomic sizes in solid solution. As a result, the standard deviation of atomic radius for each alloy is critical for determining mechanical properties. The atomic radius's standard deviation can be computed as follows:

$$s = \sqrt{\sum_{i=1}^{n} x_i (r_i - \bar{r})^2} \qquad (3.2)$$

$$\bar{r} = \sum_{i=1}^{n} r_i \, x_i \qquad (3.3)$$

where x_i is the mole fraction of element i and r_i is the atomic radius of element i. (Table 4)

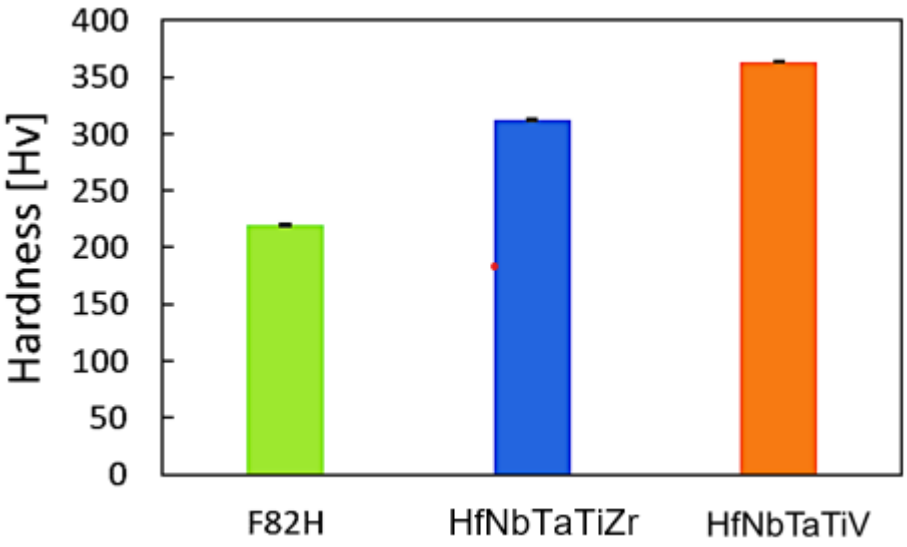

Fig. 4.5 Vickers hardness of HfNbTaTiV, Senkov alloy, and F82H.

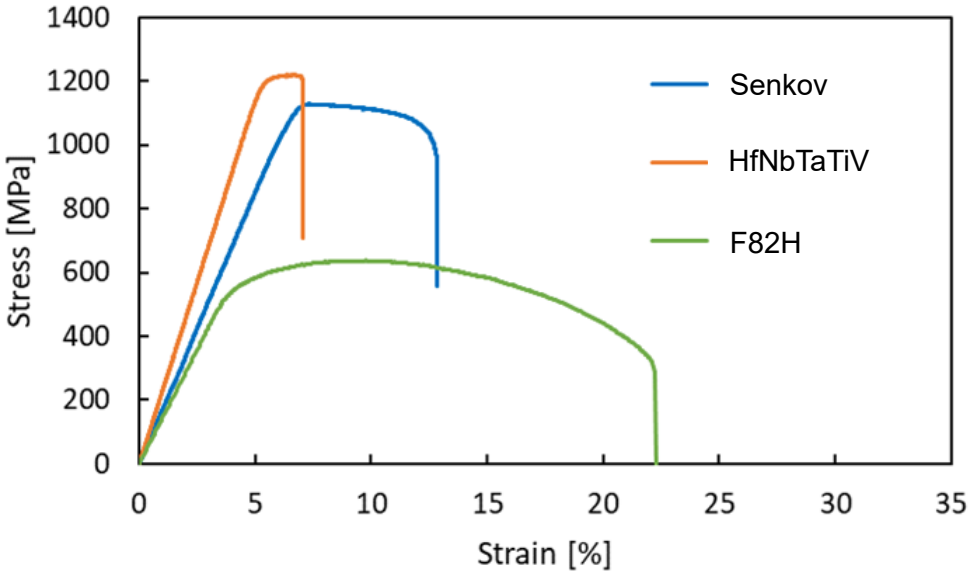

Fig. 4.6 Stress-strain curves of HfNbTaTiV, Senkov alloy, and F82H.

Table 4.5 shows the results of the standard deviation of the atomic radius for each alloy. The standard deviation of the atomic radius is higher for HfNbTaTiV than for Senkov alloy. Consequently, the increased yield stress and Vickers hardness in HfNbTaTiV alloy can be attributable to the increased lattice strain.

Table 4.4. Atomic radius for pure elements (pm)

Ti	V	Zr	Nb	Hf	Ta
141.8	131.6	155.1	142.9	154.1	143.0

Table 4.5. The standard deviation of the atomic radius for HfNbTaTiV and Senkov alloy (pm)

HfNbTaTiV	7.19
Senkov alloy	5.92

4.5 The results of nano-indentation

The results of the nano-indentation for each alloy at 100, 200, and 250 nm were shown in Fig. 4.7. The nano-hardness of unirradiated HfNbTaTiV, Senkov alloy, and F82H follows the same tendency of Vickers hardness and yield stress. In the irradiated area, however, the indentation hardness of Senkov alloy was higher than that of HfNbTaTiV. Fig. 4.8 showed the change in nano-hardness during the nano-indentation test, indicating that the irradiation hardening of the Senkov alloy is higher than that of HfNbTaTiV and F82H.

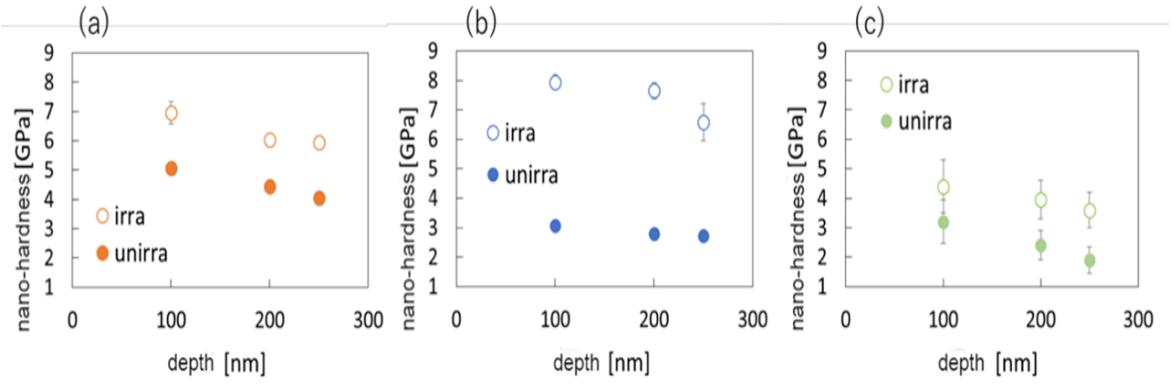

Fig. 4.7 Nano-hardness of HfNbTaTiV, Senkov, and F82H before and after irradiation.

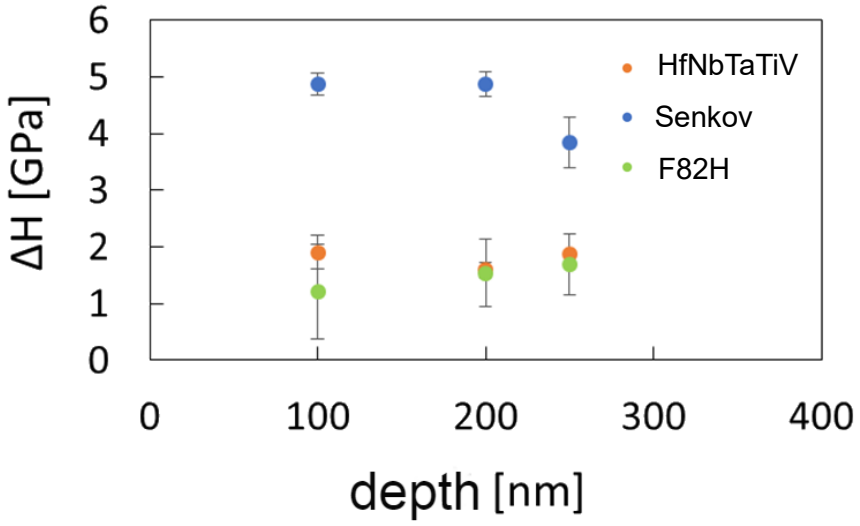

Fig. 4.8 The nano-hardness change of HfNbTaTiV, Senkov, and F82H before and after irradiation.

4.6 Irradiation effects on microstructure and discussion

Microstructural analysis using TEM was performed for all the irradiated alloys. Typical damaged microstructure of each alloy was shown in Fig. 4.9. Irradiation-induced defect clusters such as black dots and dislocation loops were observed in matrix with a high number density. The size distribution of those defect clusters was shown in Fig. 4.10. The number density and the average size of defect clusters were estimated to be 3.4×1022 and 5.9 nm, 5.7×1022 and 7.4 nm, 4.0×1022 and 5.0 nm for HfNbTaTiV, Senkov alloy, and F82H, respectively.

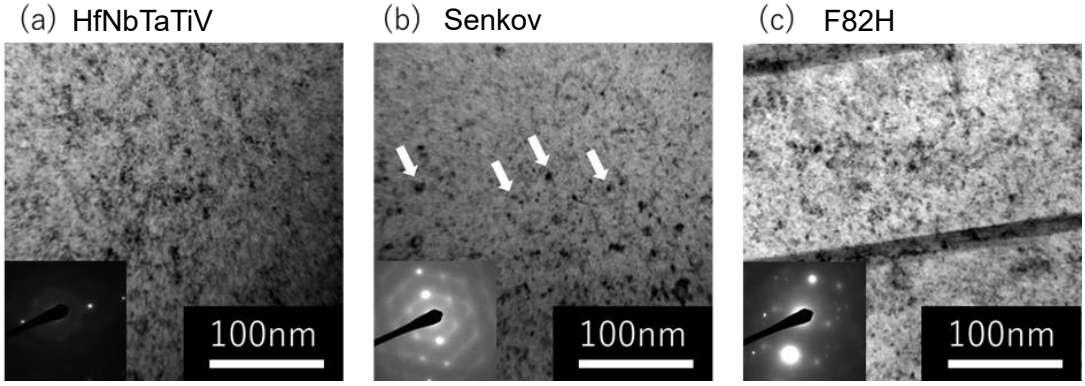

Fig. 4.9 Bright-field image under TEM observation of HfNbTaTiV, Senkov, and F82H after irradiation.

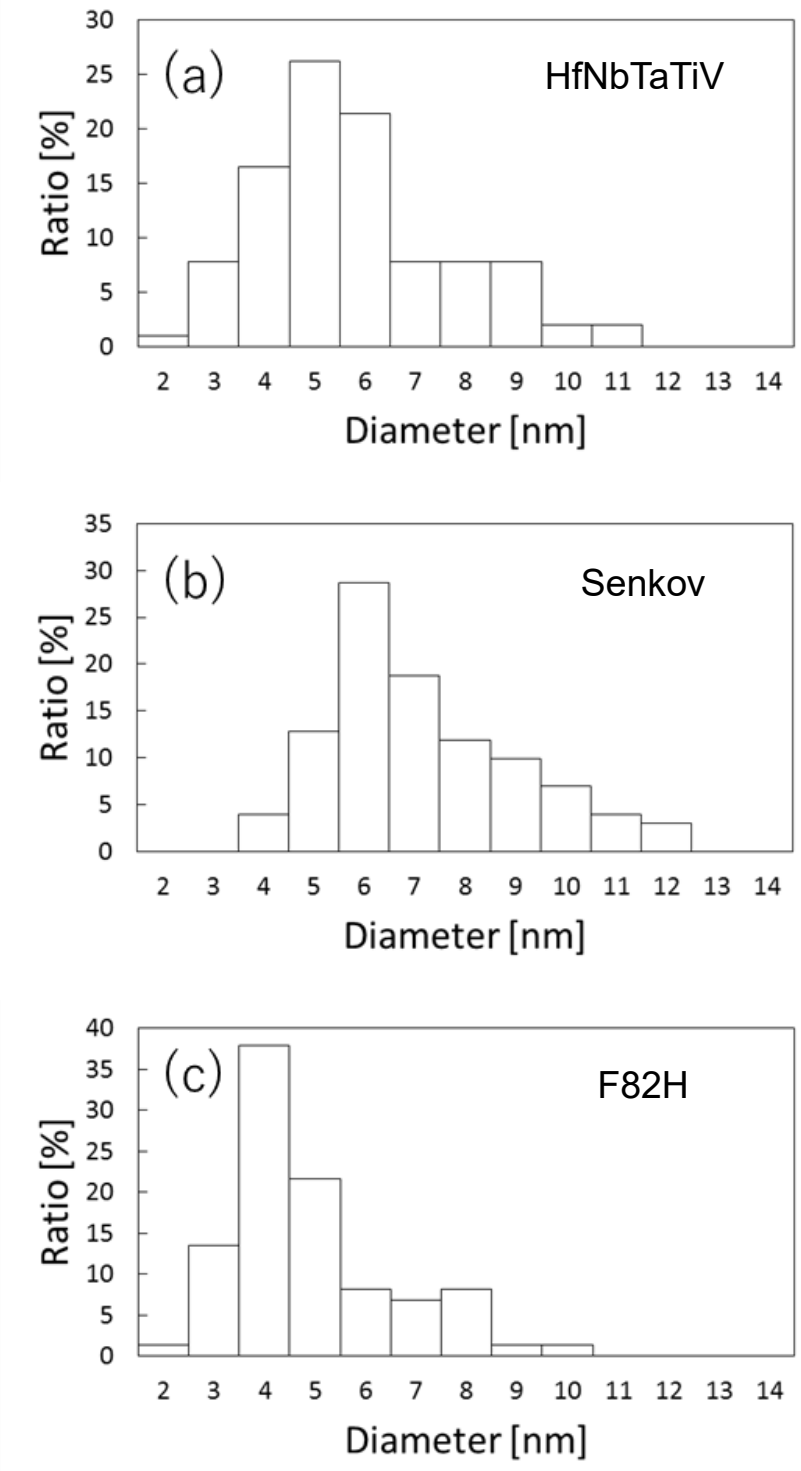

Fig. 4.10 Average size and number density of irradiation defects for HfNbTaTiV, Senkov, and F82H.

The irradiation hardening rates of some BCC phase HEAs were reported to be significantly lower than that of the BCC phase pure metals W and V, which indicates that some BCC phase HEAs are significantly better than the pure metals in terms of resistance to irradiation hardening. For example, the Fe-ion irradiated BCC phase refractory $W_{0.5}(TaTiVCr)_{0.5}$ showed a lower irradiation hardening rate (17.27 % at 6.5 dpa) compared to that of pure W (28.79% at 5.5 dpa). [90]. In addition, the V-ion irradiation at 500 ℃ to the BCC phase refractory TiVNbTa HEA resulted in the significantly less irradiation hardening rate (8.46% at 3.6 dpa) than that of the pure V (36.96% at 3.6 dpa) [91]. Furthermore, Lu et al. [92] found that as the irradiation damage of the BCC phase refractory $Ti2ZrHfV_{0.5}Mo_{0.2}$ HEA reached 0.005, 0.01 and 0.03 dpa at 600 ℃, there was no irradiation hardening phenomenon and the hardness increment and hardening rate were zero for the alloy.

The other bcc MoNbTa-based high-entropy alloys (MoNbTaTiW, MoNbTaTi, MoNbTaW) were also compared with pure W in the aspect of irradiation resistance [93], indicating that the irradiation hardening of refractory bcc HEAs are smaller than that of pure W. All those results suggests that BCC phase refractory HEAs including HfNbTaTiV would be possible candidate materials for future nuclear reactor applications. In fact, it was reported that Senkov alloy exhibited excellent overall radiation tolerance, such as irradiation-induced swelling and hardening against high-dosage damage [26]. In this study, HfNbTaTiV indicated a better irradiation hardening resistance than Senkov alloy and comparable to F82H due to less irradiation damage. Future work should study the cavity formation behavior in HfNbTaTiV irradiated at higher temperature with a higher fluences to confirm applicability to future nuclear reactor components.

4.7 Summary

Refractory high-entropy alloys: HfNbTaTiV and senkov alloy were produced by vacuum arc melting with pure metals and irradiated with F82H by DuET with 6.4 MeV Fe^{3+} at 300℃. After homogeneous heating, HfNbTaTiV and Senkov alloys have a BCC single-phase crystal structure. Vickers hardness and yield stress follow the same trend, with higher values in the order of F82H, Senkov alloy, and HfNbTaTiV. It is inferred that the lattice strain caused by the types of constituent elements contributes to the difference in Vickers hardness and yield stress. Consistent with the TEM microstructure observation, HfNbTaTiV would have a greater irradiation resistance than Senkov alloy and comparable to F82H due to less irradiation damage in this irradiation condition.

Chapter 5

Conclusions and future work

Chapter 5. Conclusions and future work

High-entropy alloys have attracted the great interest around the world because of their distinctive compositions and properties, and hence the wide realm of compositions. There are lots of literatures talking about the superior mechanical properties and high temperature properties of high-entropy alloys. However, high-entropy alloy is a very young and recent definition which lacks the evidence on the effect of multiplication elements on microstructures and properties, especially on irradiation behavior. Currently, there are some kinds of literature talking about the irradiation resistance of the FCC HEAs, but still few research talks about BCC HEAs. Therefore, in this research, we have created some refractory high-entropy alloys and we have done some irradiation work to compare the RHEAs with pure tungsten or F82H to figure out their irradiation resistance.

The work presented in Chapter 3 was performed on Refractory high-entropy alloys: MoNbTaW, MoNbTaTi, MoNbTaTiW produced by vacuum arc melting with pure metals and irradiated by DUET with 6.4 MeV Fe^{3+} at 500℃. After heat treatment at 1200°C or 1500°C, the three HEAs transformed into single-phase bcc alloys. The average Vickers hardness of three alloys was almost the same after annealing at 1500°C or 1200°C, indicating that they exhibit high-temperature stability (MoNbTaW: 550 Hv, MoNbTaTi: 420 Hv, MoNbTaTiW: 479 Hv). From the Nix-Gao model result, the irradiation hardening of MoNbTaTiW is less than that of MoNbTaTi, possibly because of the high entropy effect. There is no noticeable irradiation hardening of MoNbTaW. At a depth of 350nm, the irradiation hardening of MoNbTaTi and MoNbTaTiW was less than that of pure W. (peak region). But the TEM observation for these irradiated specimens is lacked in this research, the analysis between nano-indentation result and TEM images is required in later research.

In Chapter 4, we talk about the refractory high-entropy alloys: HfNbTaTiV and senkov alloy produced by vacuum arc melting with pure metals and irradiated with F82H by

DuET with 6.4 MeV Fe^{3+} at 300℃. After homogeneous heating, HfNbTaTiV and Senkov alloys have a BCC single-phase crystal structure. Vickers hardness and yield stress follow the same trend, with higher values in the order of F82H, Senkov alloy, and HfNbTaTiV. It is inferred that the lattice strain caused by the types of constituent elements contributes to the difference in Vickers hardness and yield stress. Consistent with the TEM microstructure observation, HfNbTaTiV would have a greater irradiation resistance than Senkov alloy and comparable to F82H due to less irradiation damage in this irradiation condition.

Both chapters have described that RHEAs have better irradiation resistance compared with pure tungsten and F82H, providing good evidence that RHEAs have great potential to be applied in high-temperature and high resistance in the future. At the same time, adjusting the composition of Titanium in RHEAs can be considered to optimize alloy mechanical properties. At the same time, the TEM observations can be very important for the future experiment to analyze the effect of irradiation on microstructures and properties of high-entropy alloys, which can also be study with nano-indentation results. Furthermore, study the cavity formation behavior in HfNbTaTiV irradiated at higher temperature with a higher fluences is also necessary to confirm if its suitable for future application in high temperature, high resistance, and high irradiation environment of the fusion reactor.

References:

[1] Chepeliev M, van der Mensbrugghe D. Global fossil-fuel subsidy reform and Paris Agreement. Energy Economics, (2020) 85:104598

[2] ARB. Soutter, R. Mõttus, "Global warming" versus "climate change": A replication on the association between political self-identification, question wording, and environmental belief, Journal of Environmental Psychology 69(2020) 101413.

[3] U. EIA. Updated capital cost estimates for electricity generation plants, US Energy Information Administration, Office of Energy Analysis, Washington, DC, USA (2010).

[4] Nuclear power reactors in the world. Fuel and energy Abstracts. 36(1995) 340.

[5] T. Allen, J. Busby, M. Meyer, et.al Materials challenges for nuclear systems, Materials today 13(2010) 14-23.

[6] J. P. Holdren. FUSION ENERGY IN CONTEXT – ITS FITNESS FOR LONG-TERM, Science 200(1978) 168-180

[7] T. Tanabe. Tritium issues to be solved for establishment of a fusion reactor, Fusion Engineering and Design 87(2012) 722-727.

[8] C. Freudenrich. How Nuclear Fusion Reactors Work, (2005). https://science.howstuffworks.com/fusion-reactor.html.

[9] F. Dorbran. Fusion energy conversion in magnetically confined plasma reactors, Progress in Nuclear Energy 60(2012) 89-116.

[10] ITER Technical Basis. Plant Description Document. G A0 FDR 1 01-07-13 R1.0

[11] J. F. Clarke. THE NEXT STEP IN FUSION – WHAT IT IS AND HOW IT IS BEING TAKEN, Science 210(1980) 967-972.

[12] Non-ferrous metals, Materials and Corrosion 43(1992) 160-167.

[13] I. V. Gorynin, V. A. Ignatov, et al. Effect of neutron-irradiation on properties of refractory-metals, Journal of Nuclear Materials 191(1992) 421-425

[14] G. Federici, C. H. Skinner, et al. Plasma-material interactions in current tokamaks and their implications for next step fusion reactors, Nuclear Fusion 41(2001) 1967-2137.

[15] V. Barabash, G. Federici, et al. Neutron irradiation effects on plasma facing materials, Journal of Nuclear Material 283(2000) 138-146.

[16] R.E. Hummel, Understanding Materials Science, second ed., Springer-Verlag, (2004).

[17] J.W. Yeh, et al. Nanostructured High‐Entropy Alloys with Multiple Principal Elements: Novel Alloy Design Concepts and Outcomes, Advanced Engineering Materials 6 (2004) 299.

[18] B. Cantor, et al. Microstructural development in equiatomic multicomponent alloys, Materials Science and Engineering: A 213 (2004) 375–377.
[19] Y.F. Ye, et al. Design of high entropy alloys: A single-parameter thermodynamic rule, Scripta Mater 104 (2015) 53.
[20] Y.F. Ye, Q. Wang, et al. High-entropy alloy: challenges and prospects, Materials Today 19(2016) 349-362.
[21] M.C. Gao, J.W. Yeh, P.K. Liaw, et al, High-entropy alloys, Cham: Spring International Publishing (2016).
[22] K. H. Cheng, C. H. Lai, et al. Recent progress in multi-element alloy and nitride coatings sputtered from high-entropy alloy targets, Ann Chemical-Science Material 31(2006) 723–736.
[23] S. Guo, C. Ng, J. Lu, et al. Effect of valence electron concentration on stability of fcc or bcc phase in high entropy alloys, Journal of Applied Physics 109(2011), 103505.
[24] J.W. Yeh, S.K. Chen, et al. Nanostructured high-Entropy alloys with multiple principal elements: novel alloy design concepts and outcomes. Advanced Material Engineering 6 (2004) 299-303.
[25] M.H. Tsai, J.W. Yeh. High-entropy alloys: a critical review, Material Research Letters 2 (2014) 107-123.
[26] R.A. Swalin, Thermodynamics of Solids, Wiley (1962)
[27] M.C. Troparevsky, J.R. Morris, et al. Stocks Criteria for predicting the formation of single-phase high-entropy alloys, Physical Review X, 5 (2015).
[28] K. Y. Tsai, M. H. Tsai, J. W. Yeh. Sluggish diffusion in Co–Cr–Fe–Mn–Ni high-entropy alloys. Acta Material 61(2013) 4887–4897.
[21] M. H. Tsai. Physical properties of high entropy alloys, Entropy 15(2013) 5338–5345.
[29] P. Ferro, A. Saccone. Structure of intermetallic compounds and phases, Physical metallurgy. 4th ed. Amsterdam, the Netherlands: Elsevier Science B.V (1996)
[30] D.B. Miracle, O.N. Senkov, A critical review of high entropy alloys and related concepts, Acta Mater. 122 (2017) 448–511
[31] H.Y. Diao, R. Feng, et al. Fundamental deformation behavior in high-entropy alloys: An overview, Material Science 21 (2017) 252–266.
[32] B.X. Cao, T. Yang, L. Fan, et al. Refractory alloying additions on the thermal stability and mechanical properties of high-entropy alloys. Material Science and Engineering 797(2020) 140020.
[33] E.S. Panina, N. Yurchenko, S.V. Zherebtsov, et al. Structures and mechanical properties of Ti-Nb-Cr-V-Ni-Al refractory high entropy alloys. Material Science and Engineering 786(2020) 139409.

[34] Y. Fu, J. Li, H. Luo, et al. Recent advances on environmental corrosion behavior and mechanism of high-entropy alloys, Journal of Material Science and Technology 80(2021) 217-233.
[35] J.K. Jensen, B.A. Welk, R. Williams, J.M. Sosa, et al. Characterization of the microstructure of the compositionally complex alloy $Al_1Mo_{0.5}Nb_1Ta_{0.5}Ti_1Zr_1$, Scripta Materialia 121(2016), 1–4.
[36] S. Lu, X. Li, X. Liang, et al. Effect of V and Ti on the Oxidation Resistance of WMoTaNb Refractory High-Entropy Alloy at High Temperatures, Metals 12(2022), 41.
[37] F. Müller, B. Gorr, H. J. Christ, et al. On the oxidation mechanism of refractory high entropy alloys, Corrosion Science 159(2019), 108161.
[38] M.A. Melia, S.R. Whetten, R. Puckett, et al. High-throughput additive manufacturing and characterization of refractory high entropy alloys. Applied Materials Today 19 (2020), 100560.
[39] A. Günen, Tribocorrosion behavior of boronized $Co_{1.19}Cr_{1.8}6Fe_{1.30}Mn_{1.39}Ni_{1.05}Al_{0.17}B_{0.04}$ high entropy alloy, Surface and Coatings Technology 421 (2021), 127426.
[40] M.S. Karakaş, A. Günen, C. Çarboğa, et al. Microstructure, some mechanical properties and tribocorrosion wear behavior of boronized $Al_{0.07}Co_{1.26}Cr_{1.80}Fe_{1.42}Mn_{1.35}Ni_{1.10}$ high entropy alloy, Journal of Alloys Compounds 886(2021), 161222.
[41] R. J. Scales, D. Armstrong, A.J. Wilkinson, et al. On the brittle-to-ductile transition of the as-cast TiVNbTa refractory high-entropy alloy, Materialia 14 (2020), 100940.
[42] M. Wang, Z. Ma, Z. Xu, et al. Microstructures and mechanical properties of HfNbTaTiZrW and HfNbTaTiZrMoW refractory high-entropy alloys, Journal of Alloys Compounds 803(2019), 778–785.
[43] Y.P. Wang, B.S. Li, M.X. Ren, et al. Microstructure and compressive properties of AlCrFeCoNi high entropy alloy, Material Science and Engineering. A 491(2008), 154–158.
[44] George, E.P.; Curtin, W.A.; Tasan, C.C. High entropy alloys: A focused review of mechanical properties and deformation mechanisms. Acta Mater. 2020, 188, 435–474. [Google Scholar] [CrossRef]
[45] Senkov, O.N.; Wilks, G.B.; Miracle, D.B.; Chuang, C.P.; Liaw, P.K. Refractory high-entropy alloys. Intermetallics 2010, 18, 1758–1765.
[46] O.N. Senkov, G. B. Wilks, et al. Mechanical properties of $Nb_{25}Mo_{25}Ta_{25}W_{25}$ and $V_{20}Nb_{20}Mo_{20}Ta_{20}W_{20}$ refractory high entropy alloys, Intermetallics 19(2011) 698–706.
[47] B. Zhang, M.C. Gao, Y. Zhang, et al. Senary refractory high entropy alloy MoNbTaTiVW, Material Science and Technology 31(2015), 1207–1213.

[48] O.N. Senkov, S.V. Senkova, D.B. Miracle, et al. Mechanical properties of low-density, refractory multi-principal element alloys of the Cr–Nb–Ti–V–Zr system, Material Science and Engineering. A 565(2013), 51–62.
[49] Senkov, O.N.; Senkova, S.V.; Woodward, C.; Miracle, D.B. Low-density, refractory multi-principal element alloys of the Cr–Nb–Ti–V–Zr system: Microstructure and phase analysis. Acta Mater. 2013, 61, 1545–1557.
[50] M.G. Poletti, G. Fiore, B.A. Szost, et al. Search for high entropy alloys in the X-NbTaTiZr systems (X=Al, Cr, V, Sn), Journal of Alloys Compounds 620(2015), 283–288.
[51] N.D. Stepanov, D.G. Shaysultanov, G.A. Salishchev, et al. Structure and mechanical properties of a light-weight AlNbTiV high entropy alloy, Material Letters 142(2015), 153–155.
[52] M. Liao, Y. Liu, L. Min, et al. Alloying effect on phase stability, elastic and thermodynamic properties of Nb-Ti-V-Zr high entropy alloy. Intermetallics 101(2018), 152–164.
[53] M. Liao, Y. Liu, P. Cui, et al. Modeling of alloying effect on elastic properties in BCC Nb-Ti-V-Zr solid solution: From unary to quaternary, Computational Materials Science 172(2020), 109289.
[54] Z.D. Han, N. Chen, S.F. Zhao, et al. Effect of Ti additions on mechanical properties of NbMoTaW and VNbMoTaW refractory high entropy alloys. Intermetallics 84(2017), 153–157.
[55] O.N. Senkov, S.V. Senkova, C. Woodward, Effect of aluminum on the microstructure and properties of two refractory high-entropy alloys, Acta Material 68(2014), 214–228.
[56] Y. Zhang, Y.J. Zhou, J.P. Lin, et al. Solid-solution phase fromatipn rules for multi-component alloys, Advanced Engineering Material, 10 (2008), 534-538
[57] C.Y. Cheng, Y.C. Yang, Y.Z. Zhong, et al. Physical metallurgy of concentrated solid solutions from low-entropy to high-entropy alloys, Current Opinion in Solid State and Materials Science 21 (2017), 299-311
[58] M.J. Jhong, I. L. Jen, K.K. Wang, et al. Nano-structure to Laves phase: Reduced Thermal Conductivity from Medium-Entropy AlNbV to High-Entropy AlNbVCrTi Alloys, Materialia 14(2020), 100889
[59] M. Sadeghilaridjani, A. Ayyagari, S. Muskeri, et al. Ion irradiation response and mechanical behavior of reduced activity high entropy alloy, Journal of Nuclear Materials 529(2020), 151955.
[60] D. Kiener, A.M. Minor, O. Anderoglu, et al. Application of small-scale testing for investigation of ion-beam-irradiated materials, Journal of Materials Research 27 (2012), 2724-2736

[61] M.C. Gao, O.N. Dogan, P. King, A.D. Rollett, M. Widom, The first-principles design of ductile refractory alloys, JOM 60 (2008) 61-65.
[62] M.C. Gao, Y. Suzuki, H. Schweiger, et al. Widom, Phase stability and elastic properties of Cr-V alloys, J Phys Condens Matter 25 (2013)
[63] H.W. Yao, J.W. Qiao, J.A. Hawk, H.F. Zhou, M.W. Chen, M.C. Gao. Mechanical properties of refractory high-entropy alloys: Experiments and modeling, Journal of Alloys and Compounds 696 (2017) 1139-1150
[64] J.I. Goldstein, D.E. Newbury, P. Echlin, et al. Scanning Electron Microscopy and X-Ray Microanalysis: A Text for Biologists, Materials Scientists, and Geologists, New York, Plenum Publishing corporation (1981).
[65] R.L. Smith, G.E. Sandland. An Accurate Method of Determining the Hardness of Metals, with Particular Reference to Those of a High Degree of Hardness, Proceedings of the Institution of Mechanical Engineers, 1(1922) 623–641.
[66] J. P. Biersack, L. G. Haggmark. A Monte Carlo computer program for the transport of energetic ions in amorphous targets, Nuclear Instruments and Methods 174(1980) 257–269.
[67] J. F. Ziegler, J. P. Biersack, U. Littmark. The Stopping and Range of Ions in Matter, New York: Pergamon Press (1985).
[68] M. Robinson, I. Torrens. Computer simulation of atomic-displacement cascades in solids in the binary-collision approximation, Physical Review B 9 (1974) 5008–5024.
[69] R. Smith, et al. Atomic & Ion Collisions in Solids and at Surfaces: Theory, Simulation and Applications, Cambridge, UK: Cambridge University Press (1997).
[70] Density Measurement. Available at https://www.mt.com/ch/en/home/applications/Laboratory_weighing/density-measurement.html
[71] V. Dolique, A.L. Thomann, et al. Thermal stability of AlCoCrCuFeNi high entropy alloy thin films studied by in-situ XRD analysis. Technology. 204 (2010) 1989¬1992.
[72] M.-H. Tsai, C.-W. Wang, et al. Thermal stability and performance of NbSiTaTiZr high-entropy alloy barrier for copper metallization, Journal of the Electrochemical Society, 158 (2011) H1161¬H1165
[73] Y. Lei, N. Hashimoto, S. Isobe, Cu-Containing High Entropy Alloys for Nuclear Fusion Application, Materials Transactions (2020)
[74] K.R. Lim, K.S. Lee, et al. Dual-phase high-entropy alloys for high-temperature structural applications, Journal of Alloys and Compounds,728 (2017) 1235¬1238.
[75] X. Qiu, J. Mater. Microstructure and mechanical properties of CoCrFeNiMo high-entropy alloy coatings, Journal of Materials Research and Technology (2020).

[76] Zhang W, Liaw PK, Zhang Y. A Novel Low-Activation VCrFeTaxWx (x = 0.1, 0.2, 0.3, 0.4, and 1) High-Entropy Alloys with Excellent Heat-Softening Resistance. Entropy. 2018; 20(12):951.
[77] S. Q. Wu, et al. Effect of Nb addition on microstructure and corrosion resistance of novel stainless steels fabricated by direct laser metal deposition. Materials Research Express 5 (2018) 036524.
[78] X.J. Ye, et al. Influence of Nb addition on the oxidation behavior of novel Ni-base superalloy, Corrosion Science, 185(2021)109436.
[79] M.F. Montemor, et al. The role of Mo in the chemical composition and semiconductive behaviour of oxide films formed on stainless steels. Corrosion Science 41 (1999) 17-34.
[80] Available at: https://thermocalc.com/about-us/methodology/the-calphad-methodology/
[81] Available at: http://www.srim.org
[82] R.E. Stoller, et al., On the use of SRIM for computing radiation damage exposure, Nuclear Instruments & Methods in Physics Research Section B 310 (2013) 75–80.
[83] W.C. Oliver and G.M. Pharr, An improved technique for determining hardness and elastic-modulus using load and displacement sensing indentation experiments, Journal of Materials Research 7 (1992) 1564–1583.
[84] Z, Zhang, E. Hasenhuetl, K, Yabuuchi, and A. Kimura. Evaluation of helium effect on ion irradiation hardening in pure tungsten by nano-indentation method, Nuclear Materials and Energy, 9 (2016) 539–546.
[85] Otto, F. & Yang, et al. Relative effects of enthalpy and entropy on the phase stability of equiatomic high-entropy alloys, Acta Materialia, 61 (2013), 2628–2638.
[86] Gali, Aravind & George, et al. Tensile properties of high- and medium-entropy alloys, Intermetallics, 39 (2013), 74–78.
[87] O.N. Senkov, S.L. Semiatin Microstructure and properties of a refractory high-entropy alloy after cold working, Journal of Alloys and Compounds, 649 (2015), 1110-112.
[88] Song-qin Xia, et al, Irradiation Behavior in High Entropy Alloys, Journal of Iron and Steel Research, International, 22 (2015) 879-884.
[89] O.N Senkov et al., Microstructure and Room Temperature Properties of a High-Entropy TaNbHfZrTi Alloy, Journal of Alloys and Compounds 509(2011), 6043-6048.
[90] O.A. Waseem, K.B. Woller, F.B. Sweidan, et al, Effects of Fe^{+} ion implantation on the properties of W and $W_{0.5}(TaTiVCr)_{0.5}$ for depth marker-based plasma erosion analysis, Nuclear Materials and Energy, 25 (2020) 100806.
[91] A. Kareer, J. Waite, B. Li, A. Couet, et al. Short communication: ‘Low activation, refractory, high entropy alloys for nuclear applications, Journal of Nuclear Materials, 526 (2019) 151744.

[92] Y.P. Lu, H.F. Huang, X.Z. Gao, et al. A promising new class of irradiation tolerant materials: Ti2ZrHfV0.5Mo0.2 high-entropy alloy, Journal of Materials Science & Technology, 35 (2019) 369-373.
[93] Y. Zong, N. Hashimoto, H. Oka, Study on irradiation effects of refractory bcc high-entropy alloy, Nuclear Materials and Energy 31 (2022) 101158.
[94] S. Chang, K-K Tseng, T-Y Yang, et al. Irradiation-induced swelling and hardening in HfNbTaTiZr refractory high-entropy alloy, Materials Letters 272 (2020) 127832.